

Clemson University

TigerPrints

All Theses

Theses

5-2023

A Hidden Spider Web of Roots: Utilizing Ground Penetrating Radar to Uncover Laterally Expansive Roots of an Oak Tree

Megan Lapkoff
mlapkof@clemson.edu

Follow this and additional works at: https://tigerprints.clemson.edu/all_theses



Part of the [Geological Engineering Commons](#)

Recommended Citation

Lapkoff, Megan, "A Hidden Spider Web of Roots: Utilizing Ground Penetrating Radar to Uncover Laterally Expansive Roots of an Oak Tree" (2023). *All Theses*. 4047.

https://tigerprints.clemson.edu/all_theses/4047

This Thesis is brought to you for free and open access by the Theses at TigerPrints. It has been accepted for inclusion in All Theses by an authorized administrator of TigerPrints. For more information, please contact kokeefe@clemson.edu.

A HIDDEN SPIDER WEB OF ROOTS: UTILIZING
GROUND PENETRATING RADAR TO UNCOVER
LATERALLY EXPANSIVE ROOTS OF AN OAK TREE

A Thesis Presented to The
Graduate School of Clemson University

In Partial Fulfillment of the Requirement for the Degree

Master of Science

Hydrogeology

by
Megan Lapkoff
May 2023

Accepted by:
Dr. Brady Flinchum, Committee Chair
Dr. Ronald Falta
Dr. Ravi Ravichandran

Abstract

Roots are critical to understanding tree health, subsurface biomass, and overall tree root stability. However, accessing tree roots is difficult and traditional methods used to quantify roots harm or kill the tree. Ground penetrating radar (GPR) provides a non-invasive way to characterize subsurface roots without harming the tree. GPR provides high-resolution data and the ability to collect data with high spatial coverage, making it an ideal tool for characterizing roots. GPR works by detecting contrasts in dielectric permittivity or electromagnetic (EM) velocity at interfaces between materials. Small scattering objects, like roots, generate predictable artifacts called diffraction hyperbolas. Diffraction hyperbolas will obscure subsurface structure but contain valuable information about the EM velocity of the soil because their shape depends on the mean root square of the velocity and the depth of the diffractor. We used diffraction hyperbolas to determine an average EM velocity and then used this velocity to apply a migration to remove the hyperbolas and clean up the image. We collected over 258 GPR lines at 10 cm spacing using a 500 MHz antenna. We set up the lines in three triangular grids remaining perpendicular to the radial direction centered over a large White Oak (*Quercus alba*) on Clemson's campus. We hand fit ~1800 diffraction hyperbolas to show that the soil velocity was 0.091 m/ns, much faster than the commonly assumed 0.065 m/ns for soil. We used the average velocity to apply a F-K migration to every individual profile. On each profile, we calculated the instantaneous amplitude by taking the magnitude of the Hilbert Transform because roots show up as positive bulls-eye anomalies in this domain. We build depth sections where individual roots can be seen as deep as 1.36 m and extending as far as 8.6 m away from the trunk. These profiles can then be extracted and compiled at specific depths to create depth sections. Our data support two key observations: 1) obtaining an accurate migration velocity is critical to image

roots, 2) Although improvements can still be made, GPR can be used to characterize root networks of trees with shallow (< 1.5 m) dendritic root networks. Using the methods presented in this thesis it is possible to estimate the subsurface biomass of the largest roots surrounding a given tree.

Acknowledgments

I would like to thank the members of my committee: Dr. Brady Flinchum, Dr. Ronald Falta, and Dr. Ravi Ravichandran for their guidance and support. I would also like to thank Dr. Brady Flinchum's research group for their support in listening, reading, and thinking about this work and how it connects to others work. Specifically, Rachel Uecker and Leah Topping. I would also like to thank Jennifer Briglio for her support in the GPR surveys. Lastly, I would like to thank Clemson University for allowing this survey to take place in Trustee Park.

Table of Contents

<i>Title Page.....</i>	<i>1</i>
<i>Abstract.....</i>	<i>2</i>
<i>Acknowledgments.....</i>	<i>4</i>
<i>Table of Contents.....</i>	<i>5</i>
<i>Table of Figures.....</i>	<i>7</i>
<i>1 Introduction</i>	<i>10</i>
<i>2 Methods</i>	<i>16</i>
<i>2.1 GPR Theory</i>	<i>16</i>
2.1.2 Antenna Frequency	16
2.1.3 Dielectric Permittivity.....	17
2.1.4 Diffraction Hyperbolas and Migration	19
<i>2.2 GPR Processing.....</i>	<i>27</i>
2.2.1 Dewow, Remove Mean Trace, and F-K Migration.....	28
2.2.1 Hilbert/Instantaneous Amplitudes	30
<i>2.3 GPR Data Collection</i>	<i>32</i>
2.3.1 Local Coordinate System.....	32
2.3.2 GPR Antenna Frequency	33
<i>2.4 Survey Design- Angular Grid</i>	<i>33</i>
<i>3 Site Description</i>	<i>38</i>
<i>3.1 The White Oak</i>	<i>38</i>
<i>4 Results.....</i>	<i>41</i>
<i>4.1 Velocity Analysis</i>	<i>41</i>
<i>4.2 Individual Profiles.....</i>	<i>44</i>
<i>4.3 Depth Maps</i>	<i>47</i>
<i>5 Discussion</i>	<i>53</i>
<i>5.1 Correct Migration Velocities.....</i>	<i>53</i>
<i>5.2 What should we do to increase our chances of seeing/imaging roots?</i>	<i>55</i>
<i>5.2 Tree health.....</i>	<i>57</i>
<i>5.3 Maximum Depth and Length of Root Maps.....</i>	<i>57</i>
<i>5.4 Estimating Biomass.....</i>	<i>58</i>

<i>6 Conclusions.....</i>	<i>60</i>
<i>Cited References</i>	<i>61</i>

Table of Figures

Figure 1: The left frequency (orange) shows how a lower frequency EM wave will travel to greater depths but has the potential to miss subsurface objects. However, the frequency on the right shows how a higher frequency EM wave (blue) is less likely to miss subsurface objects with its higher resolution, but it will attenuate much faster and thus not reach the same depths as the low-frequency GPR. 17

Figure 2: In (a) the T represents the transmitter while the R represents the receiver on the GPR. The arrows show how radio waves can move down and then be reflected when there is a change in the medium. On the left, a reflector point is shown as a new soil layer. This creates a flat line within the GPR data. On the right, the reflector point is still shown, but there is also a scatter point. 20

Figure 3: The same comparison is shown on the right (green and red), as they both have a velocity of 0.091 m/ns, and the same comparison is shown. The top left hyperbola (orange) and the top right hyperbola (green) have different velocities, with the left being 0.065 m/ns and the top right being 0.091 m/ns. The slower velocity hyperbola has a narrower shape versus the hyperbola with the faster velocity. 23

Figure 4: In case 1 (left) the parameters are that the velocity is 0.080 m/ns for the first layer, which has a depth of 1m. Then the velocity changes for the second layer, which is 5m in depth and has a velocity of 0.050 m/ns. In case 2 (right) the first layer is 2m in depth and has a velocity of 0.050 m/ns. Then the second layer has a depth of 3m and a velocity of 0.80 m/ns. In both cases, it can be seen how the initial velocity (black lines) acts as a step function. At the same time, the RMS velocity (blue lines) are the same as the initial velocity for the first layer but diverges in front the initial velocity in the second layer. With depth, the RMS velocity approaches the initial velocity line, but due to the nature of the equation for the RMS velocity, it does not ever reach it. 25

Figure 5: In (a), the processed GPR data is shown for line 86 of section 3 of the angular grid. In (b) the best-fit diffraction hyperbolas using the Kirchhoff Migration are shown in the dotted blue lines over the exact same data from (a). 27

Figure 6: This figure is outlining the processing flow for line 86 section 3 of the angular grid. The data in (a) is simply the data that is output from the GPR survey with no processing. A Dewow filter is applied with a window of 30 ns in (b). Then in (c) the remove mean trace process is applied with a window of 100 traces. In (d) a F-K migration is applied with a velocity of 0.091 m/ns. 30

Figure 7: In (a) the GPR data from line 86 in section 3 of the angular grid is shown with the picked hyperbolas. This is the same data as in figure 5, except that a F-K migration

has been added. In (b) the same hyperbolas are plotted as well as the same line of data. However, the data has been phase shifted with the Hilbert Transform. 32

Figure 8: In this figure the White oak tree trunk is at the center. The topography is shown with a total change in elevation of almost 4 m from the highest to the lowest point. The angular grid is shown in color, with section 1 in blue, section 2 in yellow, and then section 3 in purple..... 36

Figure 9: In this figure the tree trunk of the oak tree is shown at the center with the topography on the local coordinate system as well. Black arrows point to the trunk to root transition areas that shape the sections created in the angular grid. The arrows labeled with (b) and (c) show the perspective at which figure (b) and (c) are showing the tree trunk. Figure (b) and (c) show the structure for motion images of the actual tree trunk..... 37

Figure 10: The white oak (Quercus alba) used for this study located at Trustee Park on Clemson's Main Campus..... 40

Figure 11: In this figure (a) shows all three sections and their velocity picks are shown as a percentage of the total picks. While (b) shows the individual picks as a scatter plot in terms of the depth of the vertex of the hyperbola for each section picked and then the velocity of that hyperbola..... 43

Figure 12: In this figure two diffraction hyperbolas are shown with their vertices (black dots). They intersect and that intersection can be mistaken for a vertex of a hyperbola look-alike (red 'x') with parts of each of the actual diffraction hyperbola making it up. The dotted line shows what could be interpreted by the intersection as a hyperbola, even though it is not. This fake hyperbola will frequently have a significantly faster velocity than hyperbolas from the diffraction of energy. 44

Figure 13: In this figure (a) is identical to Figure 7 except that the diffraction hyperbola picks are not plotted. There is also an arrow that points to a high energy bullseye. However, (b) shows the trace from 10 m in the profile of (a). The blue line is the trace after processing which includes the F-K migration. The black line is the Hilbert transformed trace. Then the black arrow points to an energy package that is also highlighted in (a). In (c) it is the same setup as (a), but it is for line 84 of section 3 of the angular grid. The same energy package is highlighted by an arrow. Then (d) is the same as (b) except it is the 10 m trace from the profile of line 84 from section 3 of the angular grid. Again, the energy package at 30 ns is highlighted by an arrow..... 47

Figure 14: A depth section is shown for three depths in the survey with the x and y axis being the local coordinate system: 0.13 m (a), 0.62 m (b), and 1.02 m (c). In (a) shallow small roots can be viewed in section three close to the trunk. In (b) a clear root can be seen extending directly from the trunk in section 2. Then additionally there is a large

network of roots in section 3 at this depth. Then in (c) there are two large roots that extend to the end of the survey length in section 3..... 48

Figure 15: In this figure (a) is the depth section at 1.02 m from Figure 13. The difference being that three circles have been highlighted 2 m, 4 m, and 6 m away from the trunk. On the right these profiles along the circle are shown. The top (b) being the profile from all three sections 2 m away from the tree. Then below that the profile (c) from 4 m away from the trunk is shown. Then the bottom profile (d) is the profiles from 6 m away from the trunk. It is important to note that the x-axis on the profiles is in degrees that correspond to the standard degrees of a circle from the depth section (a). Then the y-axis of the profiles is in depth for the local coordinate system. 50

Figure 16: In (a) the depth section at 1.02 m is plotted with topography taken into consideration. Then the semicircles from Figure 14 (a) are shown with the profiles from Figure 14 (b), (c), and (d) are placed within the 3D space in their correct locations. Main roots can be seen in the depth section and then also shown where they intersect with the profiles. In (b) the same image is shown except the angle is different. 51

Figure 17: The normalization to the maximum amplitude is shown with the y axis being depth below the subsurface (shown as a negative value). Individual deep coarse roots can be located. For example, one large one at -1.00 m and 255 degrees. Others are visible as well. At the top of the profile there is a large continuous area of high amplitude. 52

Figure 18: In this figure the same data is presented in (a), (b), and (c) with different migration velocities. This not only affects the imaging but also affects the depth that the data is presented at. The correct depth section from Figure 13 (b) is shown here as (c) with the correct velocity of 0.091 m/ns and depth of 0.62 m. In (a) the depth has been changed from 0.62 m to 0.44 m with the velocity changed to 0.065 m/ns. Then in (b) the depth has been changed to 0.53 m and the velocity was altered to 0.078 m/ns. In both (a) and (b) the prominent roots that are present in (c) can be seen, but finer roots are obscured by the data being migrated with an incorrect velocity. 55

Figure 19: In (a) the depth section for 1.36 m below the subsurface is shown. Linear features that are identified as roots are shown in this depth section but not in the depth sections below it in depth. In (b) and (c) two different depth sections are shown (1.14 m and 0.60 m respectively). Both depth sections have examples of roots that extend beyond the maximum length of the survey which is 8.6 m away from the tree.. 58

1 Introduction

Trees are everywhere. We see them. We interact with them. Yet, we only see part of the tree. Hidden from view, tree roots provide the stable foundation that keeps the tree upright and extracts and moves water and nutrients from the soil to the canopy (Hanger, 1979). Trees are not only a key component of many biomes but regulate many of Earth's systems above and below ground (Brantley et al., 2011). Understanding the lateral distribution of roots can help us understand tree stability, biomass distribution concerning carbon storage, and mitigate or contain tree disease. Even though roots are only 1-2 m below the surface they are hidden from view and remain inaccessible. There is a need for high-resolution methods that can image root networks without killing or harming the tree.

Roots are used to transport and uptake water, minerals, and nutrients. Tree root networks provide a stable foundation for the tree. Trees with more laterally extensive roots can resist higher lateral loads (Lindström & Rune, 1999). Trees don't simply send out anchoring roots in all directions. When trees are subjected to consistent directional loading the roots adapt, acquiring specific geometries (Norris, 2005). Fine roots are not strong individuals, but because they comprise 20-31% of total tree biomass, they play a critical role in anchorage (Finér et al., 2011). Most fine roots are attached to the large anchorage roots. The important role of roots in anchoring trees leads to the critical question: *are the largest roots of the tree designed and organized to optimize stability?*

While anchorage is a pillar of root research, another challenging but important area of research is understanding how root biomass relates to carbon storage. The biomass of trees and their roots are critical carbon reservoirs (Birdsey et al., 1993). In terms of total percentage, 12.6% of the biomass of a tree is in the roots (Xiao et al., 2003). Understanding below-ground

biomass has had increased interest as total carbon storage has come to the forefront of multiple scientific fields. While having a small margin of error for the subsurface biomass for one tree may not have a large difference in the amount of carbon storage that this one tree can have when estimating state-wide or country-wide biomass, a small error for biomass estimation can compound into a large error in estimation. When calculating below-ground biomass it can be done either by invasive or non-invasive methods, with the two main invasive ways to estimate biomass being excavation and coring (Sochacki et al., 2017). These methods provide unequivocal access to the roots allowing for direct quantification. However, both excavation and coring are laborious, time-intensive, lead to root breakage, and often will damage or kill the trees (Addo-Danso et al., 2016). In contrast, biomass can be estimated either non-invasively using ground penetrating radar (GPR) (Barton & Montagu, 2004) or empirically using surface observable variables (Repola, 2008). All these methods aim to answer a specific question: **How much biomass is in the largest diameter roots of a well-established oak tree?**

Excavation is an invasive and common method for understanding, mapping, and analyzing tree roots (Niiyama et al., 2010). Excavation allows the roots to be seen, sampled, and mapped because they are no longer hidden from view. The relationships between the exposed roots and above-ground components allow us to predict the subsurface root structure of different species. However, excavation kills the tree and many of the roots are often broken and need to be correctly reassembled, and active in situ processes can no longer be observed (Addo-Danso et al., 2016). For some applications, this may not matter, but if the tree's health is of interest, then killing the tree is counterintuitive.

There are many sites where excavation is not possible. Under these circumstances, there is an alternative method: coring (Franco & Abrisqueta, 1997). Coring is an invasive method that

is less time-consuming and invasive than excavation but is still a direct method of estimating roots, and more specifically, root biomass. Coring works by taking a 5 cm in diameter or smaller core and extracting a column of soil around a tree. The fine roots, smaller than 2 mm are characterized and then the biomass can be calculated from the percentage of roots and biomass within the column. This is a valid way to quantify fine roots, but for coarse roots and for mapping the root system, coring is infeasible (Park & Yanai, 2007; Tennant, 1975).

Tree health is dependent on the health of the roots as well as access to water and nutrients (Mabhaudhi et al., 2016). A common challenge arborists often face is root rot. This common disease ails the roots of the tree first and has drastic effects on the agriculture and forestry industries (Ezrari et al., 2022; Su-See, 1999). Root rot can be hard to catch because roots are inaccessible. Once identified, one of the best management strategies is to prevent bridges for the root rot from spreading to surrounding trees. Bridges are areas where the roots of trees are close together and the disease can spread from tree to tree through the root network (Irianto et al., 2006). However, the challenge remains to identify the tree's disease before it spreads to other individuals (Bodah, 2017). Due to fine roots branching from larger coarse roots, it would be beneficial to use a tool that would non-invasively (e.g., not add additional stress to the tree) that can provide a map of laterally expansive tree roots so that disease can be efficiently managed by isolated infected tree's root networks.

Roots remain at the forefront of biomass and forestry research as they are incredibly challenging to quantify compared to above-ground biomass. Due to this, and the increased need for noninvasive methods, technology has been utilized to find an improved method for quantifying and mapping tree roots. Ground penetrating radar (GPR) is a geophysical tool that uses radio waves to image the subsurface based on the dielectric permittivity of the contents of

the subsurface. It has been used in a variety of studies with large success in locating subsurface objects as well as providing noninvasive ways to understand what structures are located below the surface.

GPR is well known in archeology targeting ancient objects within the subsurface. In Brazil, 113 GPR lines were done at 200 MHz and 400 MHz in an area suspected to have archaeological objects of interest. The objects the GPR detected varied from a fire hearth, wooden artifact, roots, and even rocks within the soil (Porsani et al., 2010). An additional study in Ancient Structures of the Valencian Cathedral in Spain found structures that were located via GPR. GPR was able to locate some of the below-ground walls and structures that were previously not known (Gracia et al., 2000). GPR has been utilized for various more modern urban and construction uses. One example of this is the use of GPR in a study to determine pavement stability. The GPR was successful in locating areas where there were higher levels of compactness, increased moisture, and void areas (J. Li et al., 2015).

The below ground features that GPR can locate are not limited to man-made ones. Soil science has also benefited from GPR (Zajícová & Chuman, 2019). Soil horizons can be detected, and the thickness estimated based on the data. This includes layers of peat and other organic layers (Zajícová & Chuman, 2019). In a study conducted in Spain, a 200 MHz GPR was used to identify specific deposits of minerals like quartz and calcite within lab samples of soil (Salat & Junge, 2010). In another study in France, GPR was used to locate compacted layers in an agricultural setting. These compacted areas are due to heavy agricultural use but are also detrimental to the health and growth of the plants that are cultivated. Ultimately, GPR was able to locate the compacted soil layers and then remediation could be carried out more efficiently and effectively (André et al., 2012).

GPR lends itself to tree root research because of its ability to image in high-resolution (easily reaching 1-2m) and cover large spatial scales. Additionally, the root structure of trees will produce strong GPR contrasts because of the moisture associated with each root. There are three main zones within each mature root. There is the maturation zone, the elongation zone, and the meristematic zone. The meristematic zone also produces the mucigel that protects the root from drying out in areas where the root pulls nutrients and water from the soil. The internal structure of the root is made up at its center of xylem and phloem – these two structures are close to fully saturated (Landsberg & Waring, 2017). Xylem is the vascular structure of the tree that transports water and soluble nutrients from the roots to other parts of the tree. Phloem is the vascular structure that transports nutrients and solutes from other parts of the tree to the roots (Roberts, 2006). The root structure described above allows the roots to stay wet. The natural structure of the roots, designed to hold water, creates a good contrast between roots and soil. These contrasts make them excellent targets for GPR.

GPR has been used to map tree roots, but it is a rare application. However, using a 450 MHz antenna, a 25 meter by 25-meter grid system with 0.05 m spacing between the lines, it is possible to map of the tree roots in relation to the crown of the tree (Hruska et al., 1999). In the United Kingdom, a tree was surveyed with 450 MHz GPR to provide a non-invasive way to monitor tree health via the roots. They used a semi-circle pattern for the lines. They were able to identify major course roots. Then a ground truthing excavation was performed to validate the GPR data (Lantini et al., 2020). GPR proves through multiple applications that it is an ideal tool for imaging the subsurface in a non-invasive way. Many situations do not allow for excavation, and GPR provides a solution for this problem. It also provides insight into what is in the

subsurface regarding anomalies and can lead excavation investigations to save time and resources.

GPR can be used for a multitude of different applications, from finding ancient archeological objects to building subsurface pipelines in a non-invasive way. It has also been used in mapping tree roots as well. The benefits of having such root maps would be a better estimation of below-ground biomass and could also be used as an assessment method for the health of trees. There are other methods of gaining root maps, but they either have high uncertainty or damage the tree. Luckily, the roots are an ideal target for GPR given their structure and the contrast of their water content versus the surrounding soil. Given that tree roots are shallow and laterally extend away from the trunk GPR provides a great opportunity to map tree roots in a non-invasive way.

2 Methods

2.1 GPR Theory

Ground penetrating radar (GPR) is a geophysical tool frequently used in urban, archeological, and geological investigations (Barzaghi et al., 2016; Conyers, 2013; Xie et al., 2018). GPR uses a transmitter to send out radio waves in the range of 10-1000 MHz. EM waves travel through the subsurface and are reflected where they can be measured on a receiving antenna. The material prosperity that causes reflections of EM waves is the dielectric permittivity (Hatch et al., 2013). It is common to use a wheel connected to the GPR that acts as the odometer recording the distance traveled and triggers the transmitting antenna at a specified distance interval. The images produced by a single GPR survey show the amplitude of the reflected energy as a function of distance along the profile relative to the transmission time. Thus, profiles are shown with distance on the x-axis and two-way travel time on the y-axis.

2.1.2 Antenna Frequency

An important parameter for GPR is the selection of the antenna's frequency. The frequency controls the resolution and depth penetration of the survey (Noon et al., 1998). Typical frequency ranges for standard GPR systems range between 50MHz to 1 GHz (Jol, 1995). Lower-frequency antennas create longer wavelengths, while higher-frequency antennas create shorter wavelengths. The wavelength of the transmitting antenna controls the resolution and depth penetration of the signal. Here resolution is determined by the ability to determine the thickness between two layers in the subsurface. Higher frequency antennas provide higher resolution, but energy is attenuated every wavelength cycle so the higher frequency the antenna, the shallower

the depth of investigation (Figure 1). The depth of penetration is an important trade off. Lower frequency antennas image deeper with lower resolution (Figure 1). A 1000 MHz antenna is going to have higher resolution, but lower maximum depths than a 250 MHz GPR antenna which will have lower resolution comparatively but reach greater maximum depths (Figure 1).

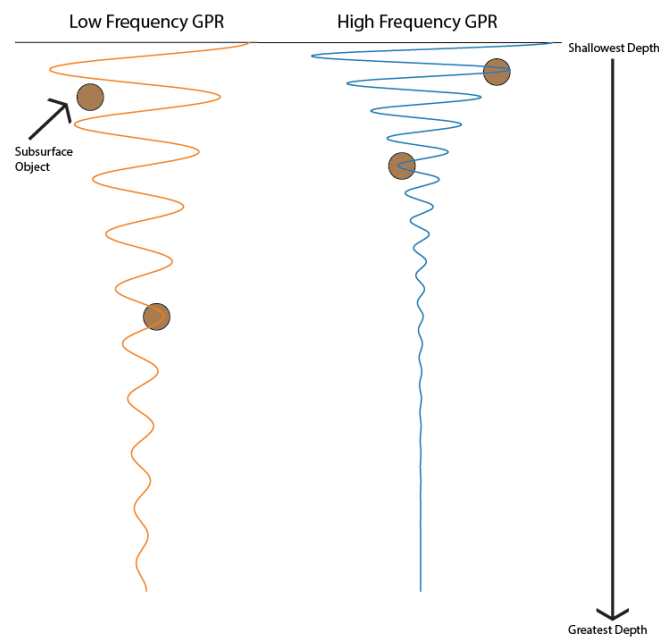


Figure 1: The left frequency (orange) shows how a lower frequency EM wave will travel to greater depths but has the potential to miss subsurface objects. However, the frequency on the right shows how a higher frequency EM wave (blue) is less likely to miss subsurface objects with its higher resolution, but it will attenuate much faster and thus not reach the same depths as the low-frequency GPR.

2.1.3 Dielectric Permittivity

Dielectric permittivity is a material property that describes how a material becomes polarized and holds a charge in the presence of an electrical field (Kaya & Fang, 1997). Since GPR fundamentally operates by propagating EM waves through a material, the difference in dielectric permittivity at interfaces will create EM reflections. The strong contrast in dielectric

permittivity between water and earth materials makes GPR sensitive to changes in water content (Topp et al., 1980). In most GPR studies, dielectric permittivity is rarely mentioned. Because all the data is relative to the start time of the transmitted EM pulse and because we pull the antenna along the ground, it is straightforward to calculate velocities (distance/time). Electromagnetic (EM) velocity is related to dielectric permittivity by:

$$V_{EM} = (\mu\epsilon)^{-\frac{1}{2}}$$

Eq. 1

Where V_{EM} is the EM velocity, μ is the magnetic permeability, and ϵ is the dielectric permittivity. Magnetic permeability and dielectric permittivity are material properties often tabled and can be found in physics textbooks (Baker et al., 2007). In GPR, it is common to express dielectric permittivity as relative permittivity so that EM velocity simplifies to (Eq 2.):

$$V = \frac{1}{\sqrt{\mu\epsilon}} = \frac{c}{\sqrt{\mu_r\epsilon_r}}$$

Eq. 2

Where μ_r is the relative magnetic permeability, ϵ_r is relative dielectric permittivity, and c is the speed of light (value of $3 * 10^8 m/s$). This can then be simplified to Equation 3 when the relative magnetic permeability is equal to 1, which can be assumed for most studies that involve non-magnetic mediums.

$$V = \frac{c}{\sqrt{\epsilon_r}}$$

Eq. 3

In GPR, most velocities are expressed in meters per nanosecond. Water has a high relative dielectric permittivity of roughly 80 while unsaturated soil has a low relative dielectric permittivity of roughly 11-36 corresponding to EM velocity of 0.033 and 0.05-0.09 m/ns (Wu et al., 2011).

2.1.4 Diffraction Hyperbolas and Migration

GPR data are collected as common-offset or common midpoint data (Forte & Pipan, 2017). Common-offset surveys are the most common because commercial radar systems are sold in a single unit that enclose both the transmitting and receiving antenna into the same box. As a result, the transmitter and receiver are always separated at a “common” distance (Neal, 2004). In a common midpoint survey the distance between the transmitting and receiver is changed so that the midpoint between the two stays the same, which provides a method to accurately estimate 1D velocities (Bradford et al., 2009; Mangel et al., 2020). All data presented in this thesis was collected with common-offset data. A key assumption with common-offset data collection is that the EM energy travels straight down and is reflected at an interface at the midpoint between the transmitter and receiver (Figure 2). In general, this assumption is satisfied for layered media and the resulting time section is like the underlying geology.

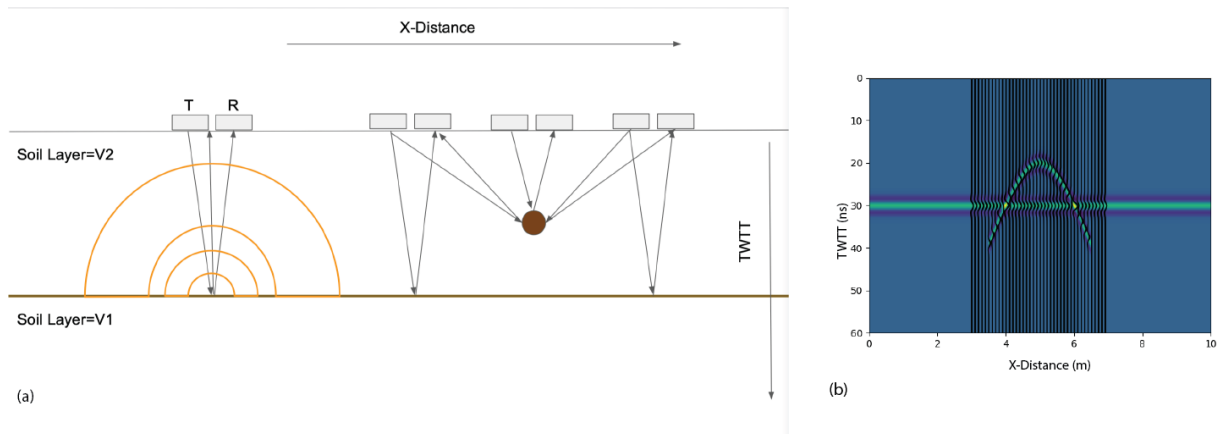


Figure 2: In (a) the T represents the transmitter while the R represents the receiver on the GPR. The arrows show how radio waves can move down and then be reflected when there is a change in the medium. On the left, a reflector point is shown as a new soil layer. This creates a flat line within the GPR data. On the right, the reflector point is still shown, but there is also a scatter point.

The common-offset assumption is that reflections are sourced from directly below the survey point (Figure 2a). The transmitted EM field radiates away from the transmitter which results in a more complex 3-D sphere if the velocity is constant. Thus, the arrival time of a reflected EM wave could come from anywhere along this spherical path. Each point along a surface act as a secondary source. When the interface is flat, the wavefronts interact constructively and produce a flat reflection in time (Figure 2b). However, if the interface is discontinuous or small, the wavefronts cannot interact constructively and this results in diffraction, or a scattering of the energy. When the energy scatters off a point source, in our case something like a core stone or a root, a diffraction hyperbola is formed in the times-section (Figure 2b). Diffraction hyperbolas are common artifacts created in common offset GPR data due to the presence of diffractors and truncated interfaces. Diffraction hyperbolas are artifacts because their reflections are not a true representation of the subsurface structure. However, the

shape and depth of diffraction hyperbolas in the common-offset sections contain valuable information about the EM velocity structure of the subsurface (Figure 2).

Characterizing the shape and depth of diffraction hyperbolas in common-offset GPR data is one way to estimate the EM velocity. The EM velocity is the keystone parameter that facilitates the transformation from two-way travel time into depth and the input parameter for migration, which removes the diffraction hyperbola artifacts before interpretation. Thus, obtaining an accurate estimate of EM velocity is vital to interpreting the data. Here we quantify EM velocity by analyzing diffraction hyperbolas from individual profiles.

The shape of the diffraction hyperbola is a function of the object's depth and the average, or in this case, root mean squared (RMS), the velocity of the material above the object. A wider aperture hyperbola indicates a faster EM velocity (Figure 3). The equation for root mean squared velocity for a layered velocity model with n layers is:

$$V_{rms} = \sqrt{\frac{\sum_{i=1}^n V_i^2 \Delta t_i}{\sum_{i=1}^n \Delta t_i}}$$

Eq. 4

V_{rms} is the root mean squared velocity, V_i is the interval velocity at the i th layer, Δt_i is the two-way travel time through the i th layer, n is the last layer, and i is the layer. The interval velocity is the true EM velocity of a given layer and cannot be measured directly with common offset data. The time at which the reflected EM energy arrives back at the GPR receiver is a function of the depth, or in this case, time, of the object and the V_{rms} (Eq. 5) velocity:

$$t^2(x) = t_0^2 + \frac{4(x-x_0)^2}{V_{rms}^2}$$

Where t_0 is the two-way travel time at the vertex of the hyperbola, x_0 is the distance along the profile where the apex of the hyperbola is located, and lastly V_{rms} is the root mean squared velocity (Eq. 4).

Using Eq. 4 and 5 we can select values of t_0 , x_0 , and v_{RMS} and calculate theoretical diffraction hyperbola (Figure 3). V_{rms} controls the aperture of the diffraction hyperbola, where faster V_{rms} values produce wider hyperbolas (Figure 3). However, t_0 also has an impact. At shallow depths, that is, small t_0 , the hyperbolas have narrower apertures than ones with the same V_{rms} sourced from deeper depths (Figure 3). We can use Eq. 5 to determine V_{rms} by visually comparing theoretical hyperbole (Figure 3) to observed hyperbole in the common-offset profiles.

The RMS velocity term can be rewritten as an *n-layered* model where each layer has a defined interval velocity. To obtain an estimate of the interval velocity, we need to have multiple RMS velocity measurements at a variety of different times (t_0). From an ensemble of the t_0 and V_{rms} picks, we can determine the overall EM velocity structure. Doing analysis this way, we can't truly measure the EM velocity because V_{rms} averages all materials above it. In other words, the V_{rms} profile should be a smooth curve even for layered models with sharp contrasts (Figure4). This provides a way to check our data, because observations of V_{rms} should not contain large changes in EM velocity over short depths (Figure 4). A common assumption with GPR data is that a single EM velocity is used to migrate and convert to depth. We will pick many diffraction hyperbolas and take the average V_{rms} and assume a single layer.

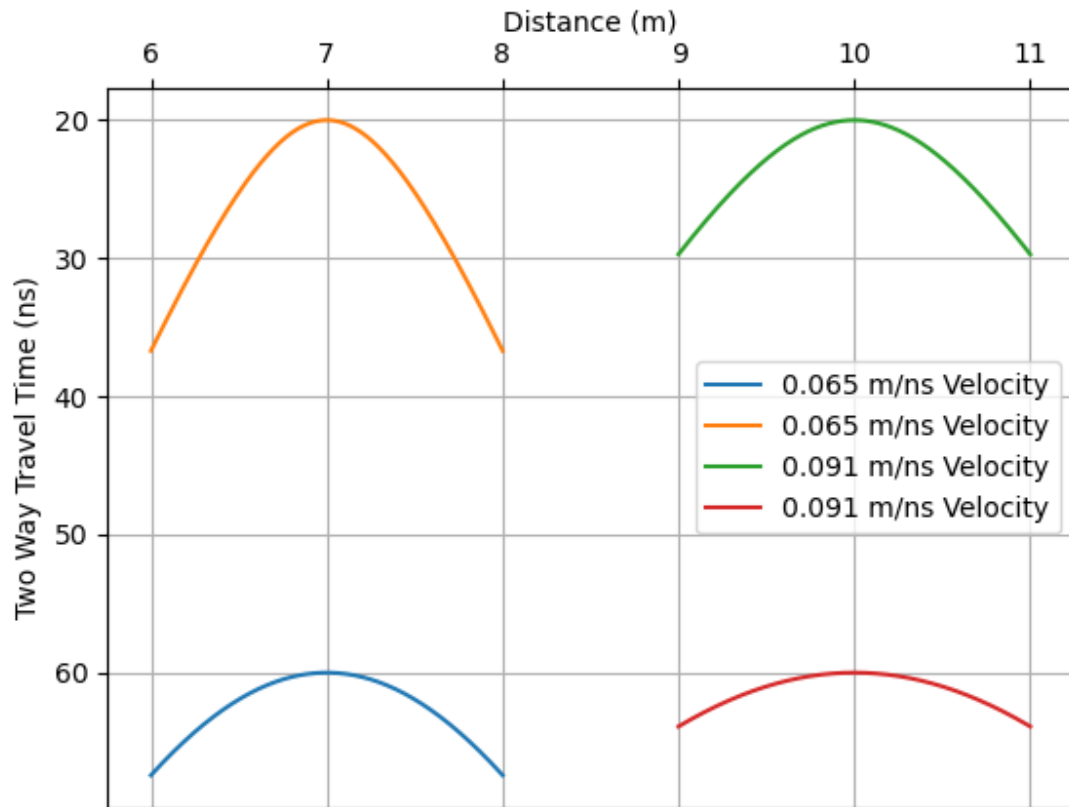
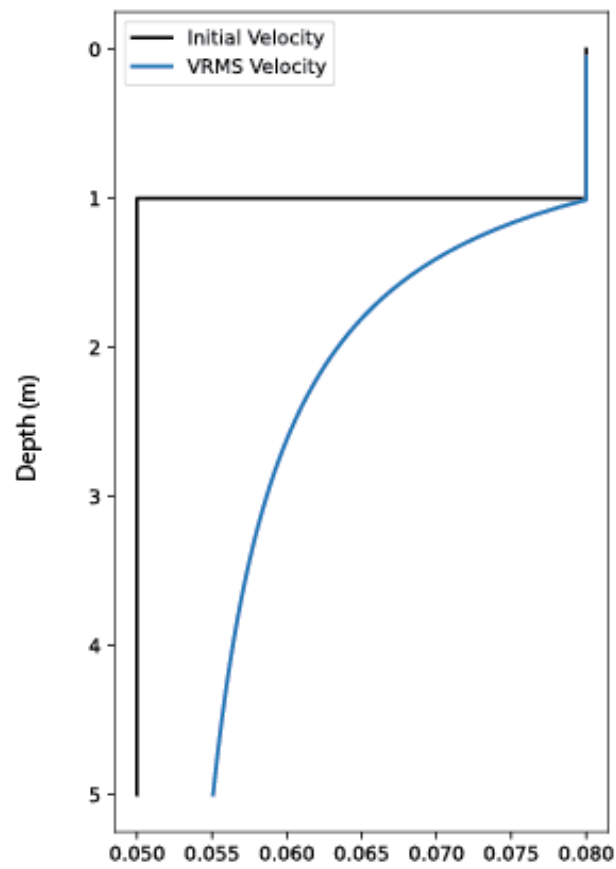
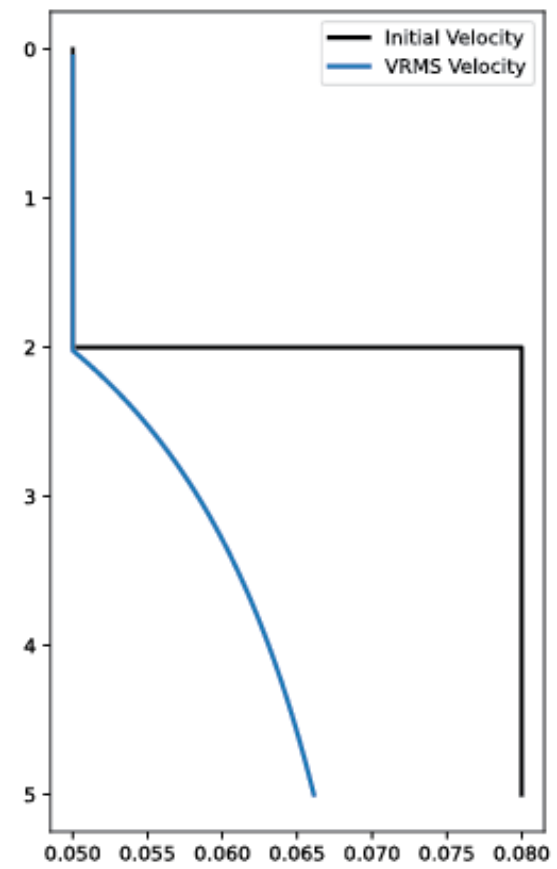


Figure 3: The same comparison is shown on the right (green and red), as they both have a velocity of 0.091 m/ns, and the same comparison is shown. The top left hyperbola (orange) and the top right hyperbola (green) have different velocities, with the left being 0.065 m/ns and the top right being 0.091 m/ns. The slower velocity hyperbola has a narrower shape versus the hyperbola with the faster velocity.

Case 1



Case 2



Velocity (m/ns)

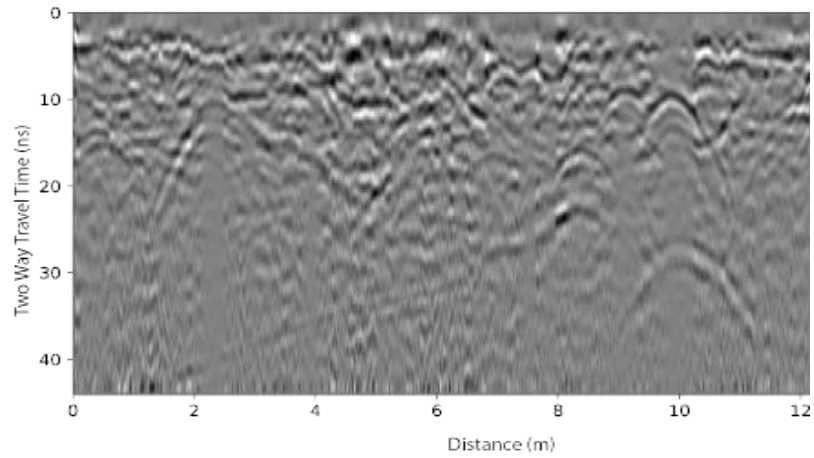
Figure 4: In case 1 (left) the parameters are that the velocity is 0.080 m/ns for the first layer, which has a depth of 1m. Then the velocity changes for the second layer, which is 5m in depth and has a velocity of 0.050 m/ns. In case 2 (right) the first layer is 2m in depth and has a velocity of 0.050 m/ns. Then the second layer has a depth of 3m and a velocity of 0.80 m/ns. In both cases, it can be seen how the initial velocity (black lines) acts as a step function. At the same time, the RMS velocity (blue lines) are the same as the initial velocity for the first layer but diverges in front the initial velocity in the second layer. With depth, the RMS velocity approaches the initial velocity line, but due to the nature of the equation for the RMS velocity, it does not ever reach it.

With Eq. 4 and 5 we can construct a good estimate of EM velocity. This velocity profile, or a single value, can be used to migrate the data (Gardner et al., 1974). Migration is the process that removes the diffraction hyperbolas by projecting the diffracted energy back to the source of the diffractor—which is usually the apex or the truncated edge of a flat-lying reflector (Moser & Howard, 2008). There are a variety of migration algorithms available but the two most common are Kirchhoff and Stolt migrations (Liu et al., 2017). Kirchhoff migration requires the true (e.g., interval velocity in Eq. 4) velocity under the profile. Using this information, the algorithm calculates a diffraction hyperbola at every location in the image and sums the energy along the hyperbola’s path. The total energy is then projected from the time domain into the depth domain. The final profile, if the velocity model is correct, is the true spatial distribution of reflectors below the profile. Kirchhoff migration is standard but is very computationally expensive (Figure 5). However, in most GPR applications, the EM velocity does not vary that much, so we can usually assume a constant half-space velocity. Under this assumption, the computation expense of migration gets significantly reduced by doing the analysis in the frequency/wavenumber

domain. This particular algorithm is known as F-K or Stolt migration, which is the most commonly applied migration scheme in GPR studies (Warren et al., 2015).

Line 86 on Section 3 of the Angular Grid
with and without highlighted hyperbolas

(a)



(b)

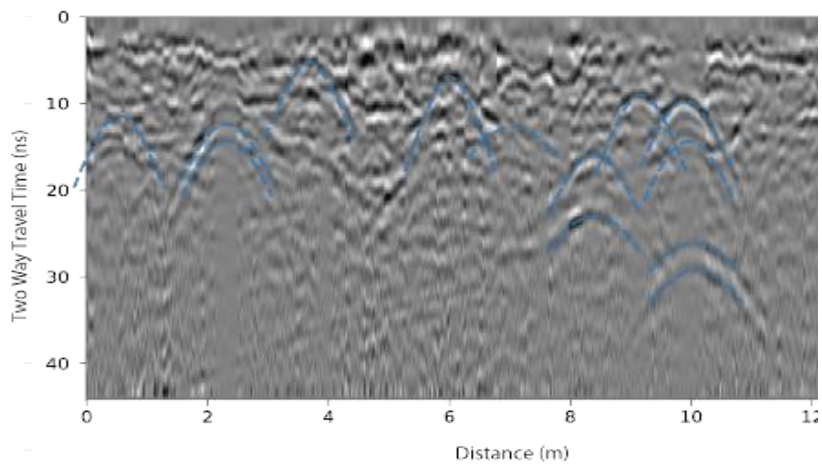


Figure 5: In (a), the processed GPR data is shown for line 86 of section 3 of the angular grid. In (b) the best-fit diffraction hyperbolas using the Kirchhoff Migration are shown in the dotted blue lines over the exact same data from (a).

When GPR data are brought in, the y-axis is in two-way travel time. To be able to know where the subsurface roots are, this axis must be transferred to a length unit. This means that the velocity must be applied to this axis. The velocity units are in meters per nanosecond and the y-axis is two-way travel time (TWTT) which has units of nanoseconds. This makes the y-axis simple to convert to a depth in meters. Then the depth of the subsurface objects can be interpreted. However, this implies the velocity directly impacts the depths as shown in Eq 6.

$$TWTT = \frac{2 * Depth}{Velocity}$$

Eq. 6

Where $TWTT$ is two-way travel time, $Depth$ is the depth of the section, and $Velocity$ is the velocity used for the F-K migration. In Eq. 6 the depth of the section is related to the velocity and the two-way travel time. This can then be used to find the same data when using different velocities. For example, compare the same data with different velocities. Utilizing Eq. 6 and three separate velocities in Figure 17 the changes in the depth are shown along with the impact that the change in velocities has in the y-axis.

2.2 GPR Processing

The general workflow for processing the GPR data is similar for all the lines of GPR data. When the processed data are downloaded from the SD card within the GPR, it is raw data. With processing, the features that the GPR picks up become highlighted. In the data, there are

two main phases of processing. The first one is the multi-step processing done before the Hilbert Transform. This includes a de-wow processing effect, removing mean traces, and lastly a F-K migration. The goal of this first phase of processing is to show diffraction hyperbolas. These highlight a point where there is an anomaly in the subsurface that has a different dielectric permittivity than the surrounding soil. The second phase of processing is the Hilbert Transform. The Hilbert Transform is a phase angle transformation, which creates a dataset that is easier to pick and identify roots along with other subsurface structures.

2.2.1 Dewow, Remove Mean Trace, and F-K Migration

Dewow is a high pass filter. What this means is that the high frequencies are allowed to pass through and be shown in the dewowed data, but the low frequencies are cut. In GPR data there is frequently a large number of low frequencies near the surface created through antenna characteristics; essentially, they are noise from the antennas. These low frequencies distort the actual data and imaging that is shown, especially in shallow depths. Therefore, dewow is used to remove this antenna noise.

We removed the mean trace to remove the air wave and initial ground wave that are at the top of the GPR profile in the raw data. The remove mean trace function works by being given a window to average. In the processing for this study a window of 100 was used which is shown in figure 6 (c). This means that the function averaged over 100 traces. Once the average is determined over the entire window then the average is subtracted from each value. This is useful for uncovering structures that are very shallow and close to the surface that might be overshadowed by these large waves from changes in the medium.

The desired effect from the first processing phase is to have diffraction hyperbolas brought out. What these diffraction hyperbolas show are locations where energy has been scattered or diffracted. At the peak of the diffraction, hyperbolas are where the subsurface anomaly is located. We use these diffractions to find the EM velocity (details below).

Lastly a F-K migration is applied to the data. This is like the Kirchhoff migration in that the end goal is to sum the energy along the diffraction hyperbola. However, the Kirchhoff migration is tedious and would be time intensive to do for each of the profiles in this study. The F-K migration provides a shortcut by taking the frequency of the GPR data into the frequency domain. Here the energy peaks are simplified and what would be complex math in the 1-D profiles, becomes simple multiplication. When the data is moved back into 1-D space the energy is represented as summed energy. This is quicker with computer programming versus the Kirchhoff migration and provides the same output that is desired to be able to track high-energy peaks that represent subsurface anomalies and potential roots. The one assumption with the F-K migration is that the subsurface had a homogenous velocity. This means that a velocity analysis must be done to find an accurate velocity that best represents the subsurface of the survey area. An application of the F-K migration is shown in figure 6 (d).

Processing Flow of GPR Profile- Line 86 Section 3 of the Angular Grid

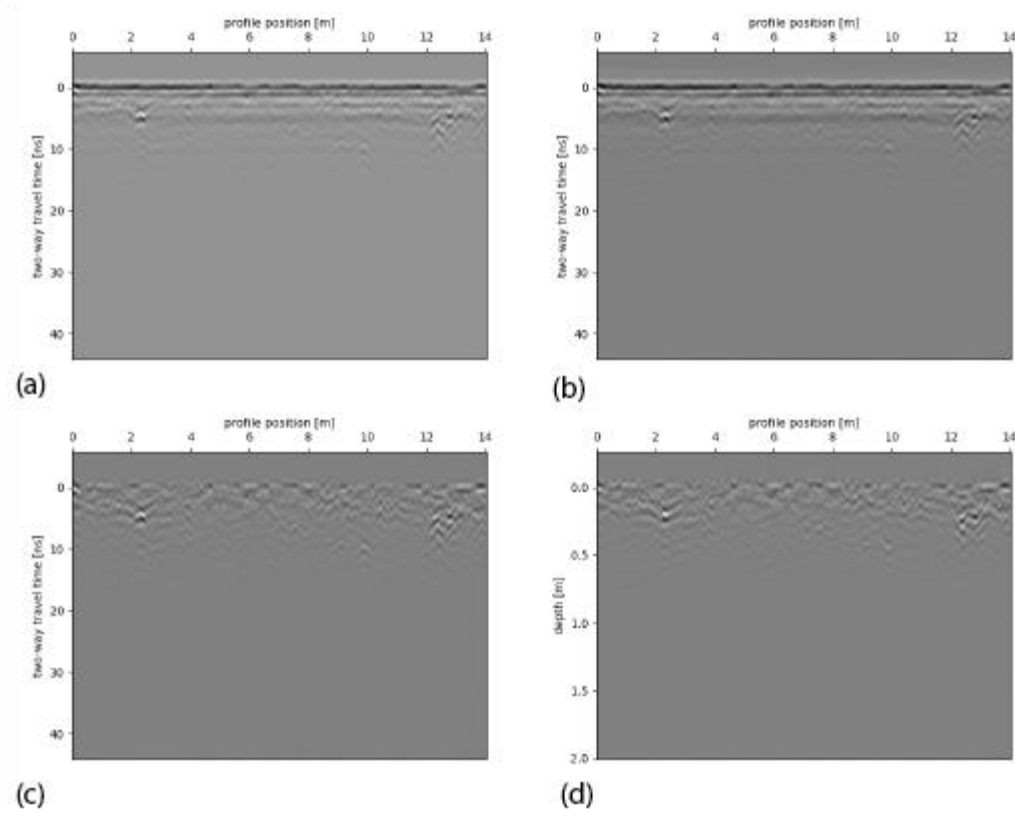


Figure 6: This figure is outlining the processing flow for line 86 section 3 of the angular grid. The data in (a) is simply the data that is output from the GPR survey with no processing. A Dewow filter is applied with a window of 30 ns in (b). Then in (c) the remove mean trace process is applied with a window of 100 traces. In (d) a F-K migration is applied with a velocity of 0.091 m/ns.

2.2.1 Hilbert/Instantaneous Amplitudes

The Hilbert Transform is a commonly utilized function within GPR processing (W. Li et al., 2018). This transformation is a phase angle transformation. This means that all the negative frequency values are turned into positive value. With the Hilbert Transform, even the negative values within a trace can be summed, like in the Kirchhoff migration, to get a total energy value and still be represented within the summation. This is important as the negative values in the

traces are just as important as positive values when showing high-energy packages. If the negative values are summed with the positive values, regardless of how high they are, a value of zero could be the result. This would not represent the data and what is being imaged in the subsurface. Therefore, the Hilbert Transform is applied to make all values within the trace positive. This makes the data easier to visualize as well as easier to pick out high energy values, which pinpoint subsurface objects. The Hilbert transform of a GPR profile is shown in Figure 7, along with a F-K migrated profile (pre-Hilbert Transform) from the same location of line 86 of section 3 of the angular grid.

The effect of the Hilbert transform is that the diffraction hyperbola is replaced with the bullseye at the vertex that corresponds to the amount of energy shown in the traces that make up the hyperbola. The bullseyes are easier to track for linear continuity. The reason that we want linear continuity with the bull's eyes throughout multiple lines of GPR data is that that structure points directly to a root. There are no other subsurface structures that they can be, especially since the roots get deeper as they extend away from the trunk, and all have a central location of the tree trunk. When multiple bullseyes line up with the features that are expected of a laterally extensive root system then the map of the tree roots starts to come together in a way that is visually easy to pick up where subsurface roots are located.

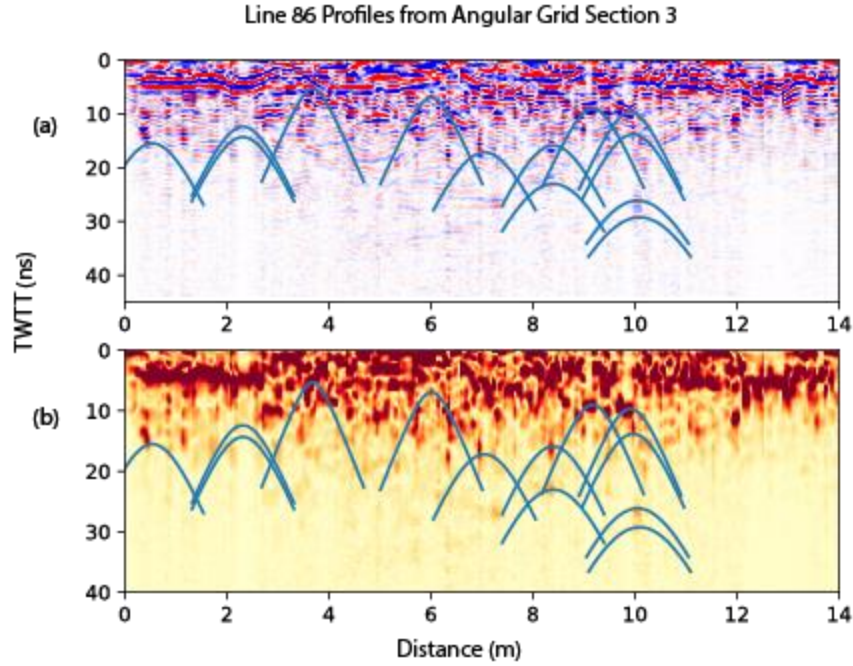


Figure 7: In (a) the GPR data from line 86 in section 3 of the angular grid is shown with the picked hyperbolas. This is the same data as in figure 5, except that a F-K migration has been added. In (b) the same hyperbolas are plotted as well as the same line of data. However, the data has been phase shifted with the Hilbert Transform.

2.3 GPR Data Collection

2.3.1 Local Coordinate System

A total station was used to create a local coordinate system. The corners of the broader survey area were surveyed in and then the corners of each triangular section were surveyed in addition. This allowed the locations for the start and end of each GPR line to be known and therefore, the data could be placed in the correct location within the local coordinates. This means that GPR lines are oriented in the actual way they were collected, and the spatial location of roots could be known.

2.3.2 GPR Antenna Frequency

The GPR antenna used for this survey was a 500 MHz frequency. This antenna was chosen due to its ability to reach depths of roughly 2 meters. The maximum rooting depth of most mature trees is around a meter but can extend up to 2 meters. This maximum rooting depth influenced the choice in antenna. The 500 MHz allows us to image to the estimated maximum rooting depth, but also doesn't overshoot the depth so that resolution is decreased necessarily. This antenna maximizes resolution while still imaging to the maximum rooting depth.

2.4 Survey Design- Angular Grid

There is no standard configuration to collect GPR lines around trees. Circular patterns have been used so that the lines remain perpendicular to the tree (Zenone et al., 2008). A circular collection is more tedious and challenging to set up than a survey with straight lines and it would be not easy to collect circles that were close together accurately. We were searching for a configuration that kept the setup simple (e.g., straight lines), would allow to collect lines close together (e.g., spatial resolution), and keep presumed radial roots perpendicular to the profiles.

We decided that a grid with small line lengths near the tree and getting larger would suffice. We called this an angular grid because the line set captures an angular region within a circle (Figure 8). This grid combined features from both rectangular and circular grids. It had the ease of setup that was desired from the rectangular grid, but it had the perpendicular lines to projected roots that were needed for the best imaging. An additional benefit was the ability to create triangular-shaped sections that best fit based on the physical structures of the trunk and tree. The trunk-to-root transition (Figure 9) areas that are located at the base of the tree were

what were used to determine the dividing points of each section (Figure 9). Two of the large trunk-to-root transition areas are highlighted in figure 9. These trunk-to-root transition areas are predictors used to estimate where large roots may be. When deciding the divide between sections, ideally, these trunk to root transition structures were in the middle of the triangular section. Once the divide between the triangular sections was determined then, lines were determined starting at the trunk and continuing out 8.6 m from the trunk at 10 cm intervals. This configuration made it so that each section had 86 GPR lines. This number of lines was determined as the canopy extended on average 8.6 m from the trunk. A total of 106 m^2 of the area was surveyed within the three triangular sections. Each section is shown in figure 8.

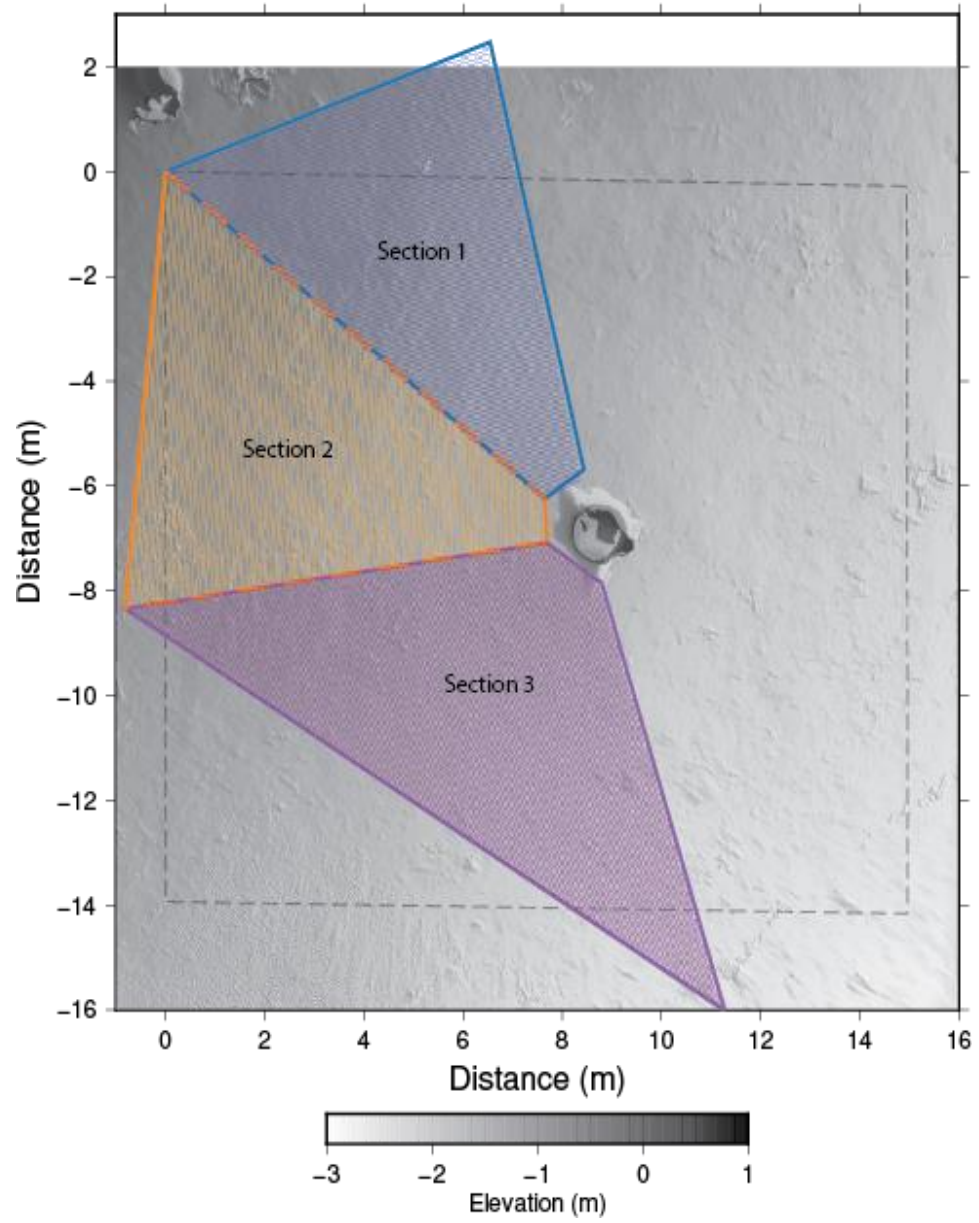


Figure 8: In this figure the White oak tree trunk is at the center. The topography is shown with a total change in elevation of almost 4 m from the highest to the lowest point. The angular grid is shown in color, with section 1 in blue, section 2 in yellow, and then section 3 in purple.

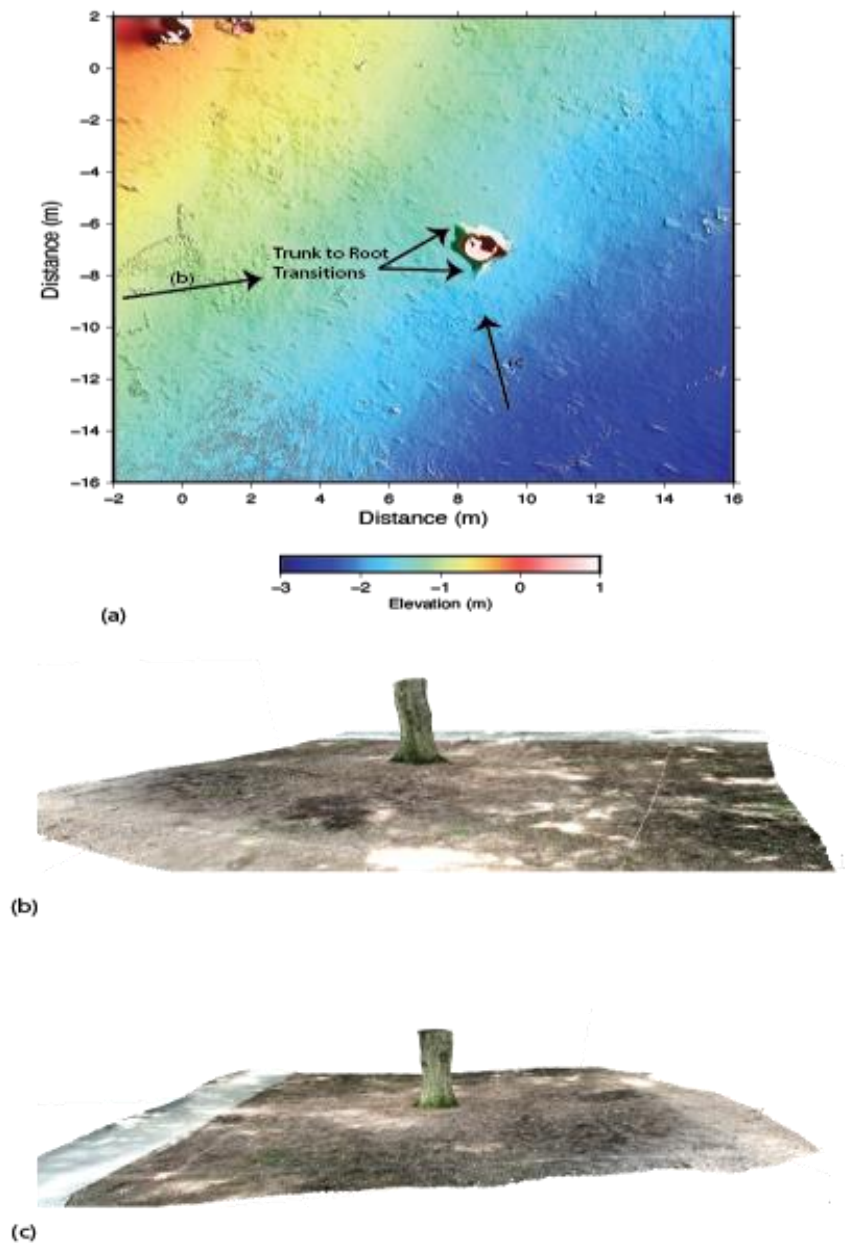


Figure 9: In this figure the tree trunk of the oak tree is shown at the center with the topography on the local coordinate system as well. Black arrows point to the trunk to root transition areas that shape the sections created in the angular grid. The arrows labeled with (b) and (c) show the perspective at which figure (b) and (c) are showing the tree trunk. Figure (b) and (c) show the structure for motion images of the actual tree trunk.

3 Site Description

3.1 The White Oak

A white oak (*Quercus Alba*) tree on Clemson's campus, within Trustee Park, was chosen as the center of the survey, given that it is isolated from other shrubs and trees. This minimizes the interaction of other roots coming into the survey area. Additionally, there is a change in topography from one side of the tree to the other. Half of the survey that has been completed is on the uphill side of the tree due the expectation that there will be more roots on that side. This is because of the understanding that trees will anchor themselves uphill for increased stability against high winds and other environmental impacts. This tree was selected due to the relative isolation, which will allow for better imaging of roots from this specific tree and the fact that this is a very mature tree and was expected to have many coarse roots present.

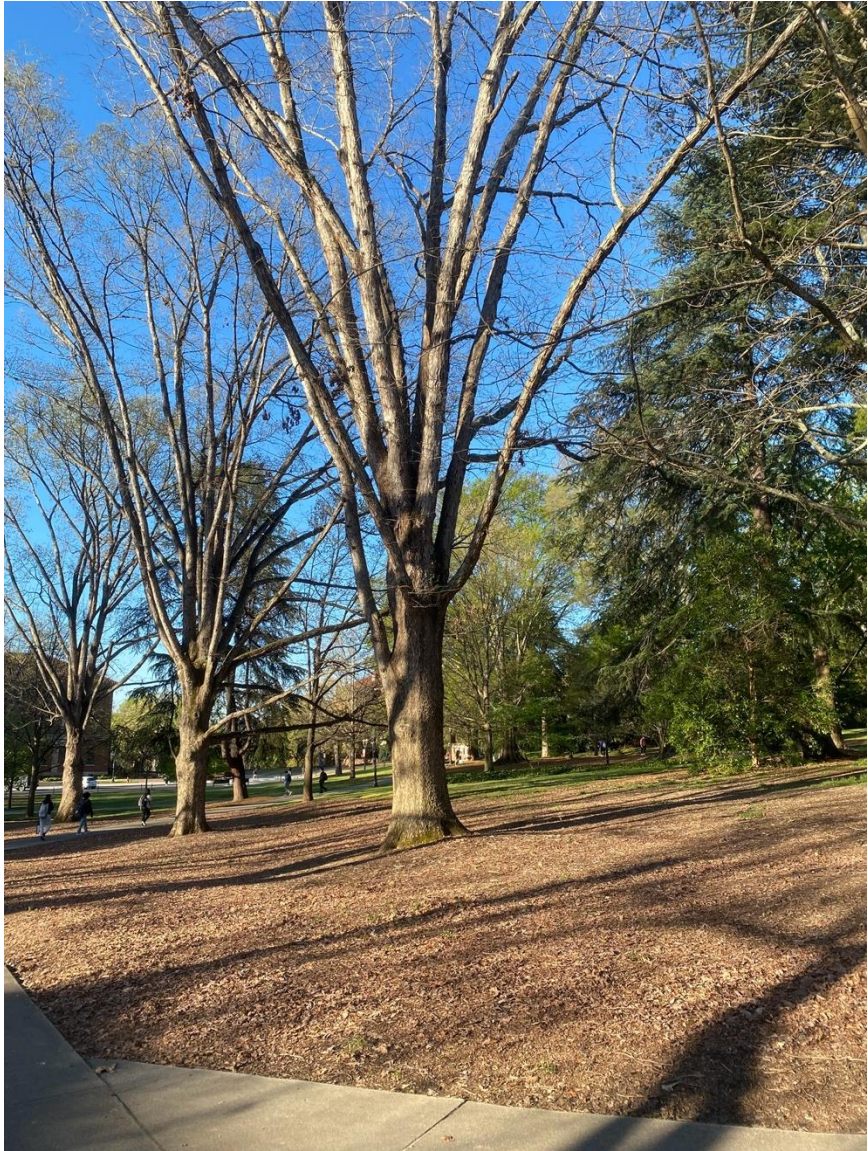


Figure 10: The white oak (*Quercus alba*) used for this study located at Trustee Park on Clemson's Main Campus.

4 Results

4.1 Velocity Analysis

Velocity analysis is critical for the identification of roots in the GPR data. The velocity changes the depth at which roots are observed and the clarity of the subsurface images. When GPR data is collected everything is relative to the transmit time, so the y-axis represents the travel time it takes for energy to travel to and from an interface. The time on the y-axis in GPR plots, although expressed in ns, is named TWTT. The x-axis is the distance from the start of the profile (m). TWTT is given in nanoseconds and can easily be converted to a depth below the subsurface if the velocity is known. For most applications, the depth to target is required. Therefore, a velocity for the area is required. However, this velocity can affect the interpretation of the depth of where anomalies are within the subsurface. In addition, due to using the F-K migration later in the processing, we must only use one velocity per layer. Therefore, a single velocity must be found that best fits the data that was collected through the survey.

We used code written in Python that calculates the theoretical diffraction curve at any given time and distance along a profile (Eq 5). A series of hyperbolas for different velocities were tried and the energy along each theoretical velocity was summed. When the velocity matches the observed fit, the sum is maximized. This semblance of a multitude of different hyperbolas allows us to pick and estimate the velocity of hyperbolas rapidly. In this study, 258 lines of GPR data were used to identify 1800 hyperbolas within the three sections of the angular grid. The velocities, as a function of their depth, computed using Eq (4) showed a depth invariant velocity of 0.091 m/ns (Figure 10). An average for each section was calculated as well as an average for the entire survey, which is the value that was used for the velocity v in the processing

of the data. It is also important to note that the data also shows that a large percentage of the velocities picked are around the survey average of 0.091 m/ns. This further confirms that this is a valid velocity for the area, as opposed to having values at both extremes of fast and slow velocities.

Velocity Analysis of Angular Grid

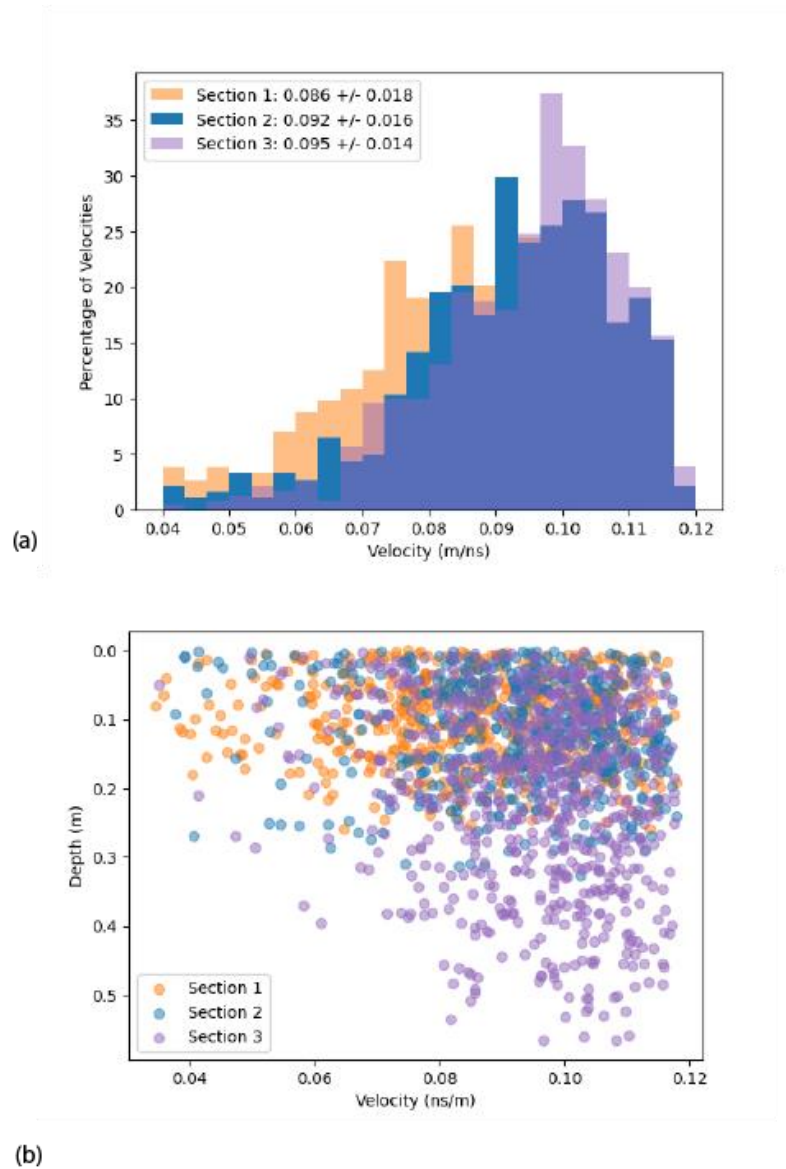


Figure 11: In this figure (a) shows all three sections and their velocity picks are shown as a percentage of the total picks. While (b) shows the individual picks as a scatter plot in terms of the depth of the vertex of the hyperbola for each section picked and then the velocity of that hyperbola.

We picked so many hyperbolas to reduce the error that is incurred from features that look like and act like diffraction hyperbolas but are not. If we were to rely on a minimal number of hyperbolas, we could easily obtain the wrong velocity. For example, if two roots were close together, which created diffraction hyperbolas where the tails cross might be misinterpreted as another, much slower, hyperbola (Figure 11). In Figure 11, an intersection point can be seen where a diffraction hyperbola pattern is present, but it is not the location of a subsurface anomaly. The cartoon in Figure 11 is an ideal case. In real data, the tails will attenuate and are complicated by other flat-lying reflections so the cross-over point might look like the strongest hyperbola. Because we used a semblance approach if we didn't pick the exact center of the diffraction the velocity would be adjusted to reach maximum semblance. To minimize these errors, we picked as many diffraction hyperbolas as possible, assuming that the average would be appropriate.

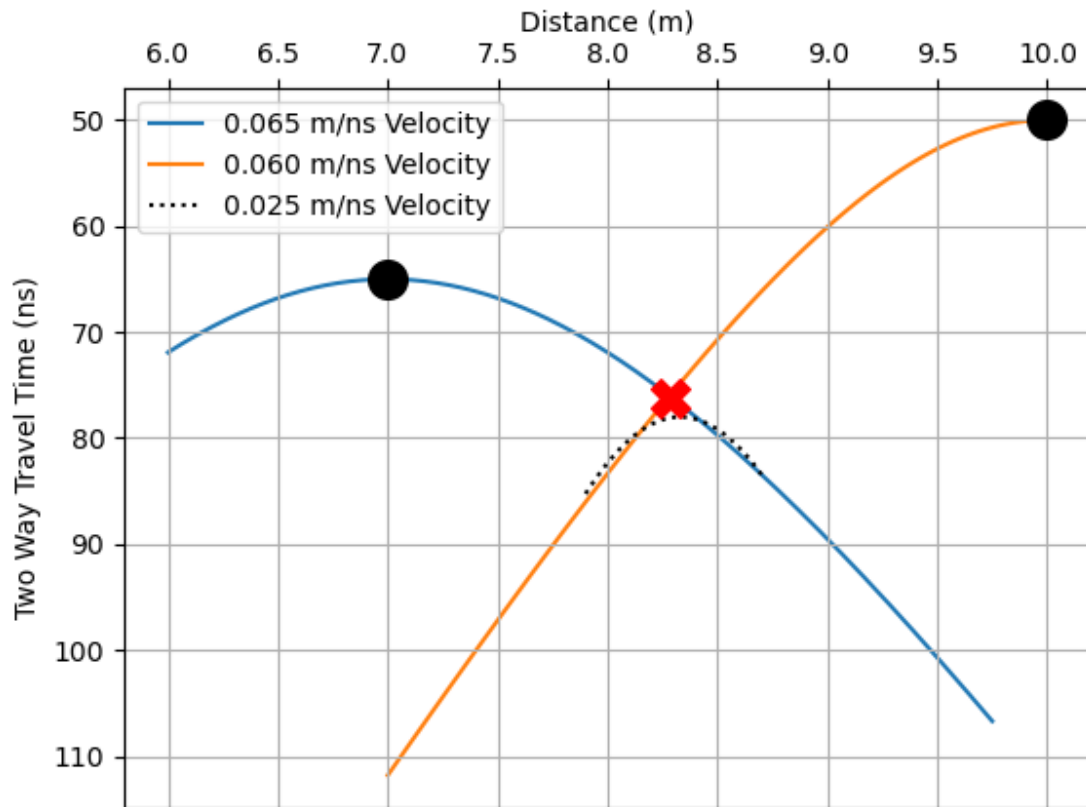


Figure 12: In this figure two diffraction hyperbolas are shown with their vertices (black dots). They intersect and that intersection can be mistaken for a vertex of a hyperbola look-alike (red 'x') with parts of each of the actual diffraction hyperbola making it up. The dotted line shows what could be interpreted by the intersection as a hyperbola, even though it is not. This fake hyperbola will frequently have a significantly faster velocity than hyperbolas from the diffraction of energy.

4.2 Hilbert Transform Profiles

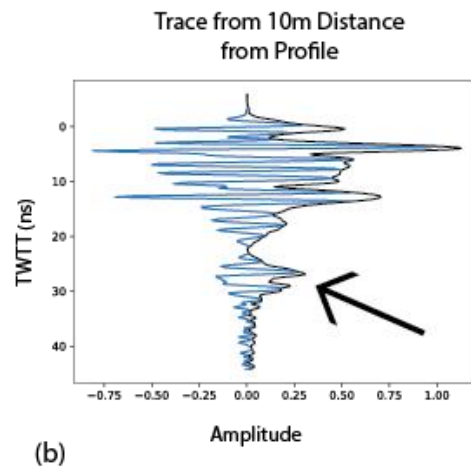
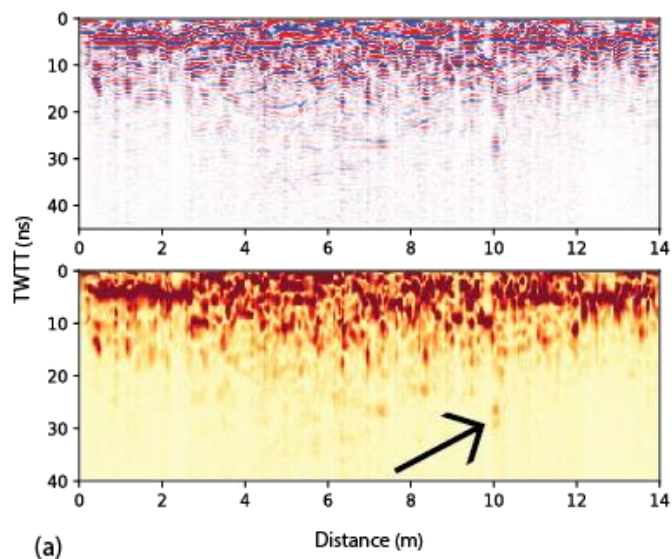
In the final F-K migrated profiles (Figure 12a), the diffraction hyperbolas are collapsed into bright single-point reflectors (Figure 12). With only a single GPR profile, it would be impossible to know if the bright reflectors were a pipe, core stone, or root. However, given the

dense data set (10 cm spacing), we know these features are roots because they can be tracked spatially across multiple profiles. The bright reflectors can be enhanced using the Hilbert transform, which caused the collapsed hyperbolas to become bright bullseyes (Figure 12c). In the Hilbert transform space, the small bright reflections are much easier to track and reduce the need to look at oscillating (negative/positive) data.

Each profile is composed of many traces. A trace from the 10m distance along the profile after the F-K migration is shown in Figure 12 (b) in blue. Energy packages, a rapid change in frequency, can be traced from trace to trace, given that these features make up the profile. When the same trace has the Hilbert transform applied (Figure 12b, black line), then all the negative amplitudes become positive. Then instead of looking for rapid changes in amplitude, we are just looking for peaks. This becomes easier visually, especially when looking at multiple profiles.

When the roots are tracked from one profile to the next, the peak in amplitude or bullseye that the Hilbert transform produces must be similar. They do not have to be exact in size or location. However, they must follow what would be plausible for a root as far as changes in location and size gave the change in the position from one profile to the next. In Figure 12 (a) to (c), many of the bullseyes can be tracked from one profile to the next in almost the same location and relatively the same size. This would be a feature, that if it continues over multiple profiles, would be a root. One of these features can be traced with the black arrow. In Figure 12 (a) the arrows are at 10 m on the profile and then 30 ns. In Figure 12 (b) that same high energy package, is seen within the trace. This feature is also seen in line 84. Figure 12 (c) also highlights that same bullseye with an arrow at 10 m along the profile and 30 ns. Again, in 12 (d) the individual trace at 10 m shows the high energy package at 30 ns along the trace.

Line 86 From Section 3 of the Angular Grid



Line 84 From Section 3 of the Angular Grid

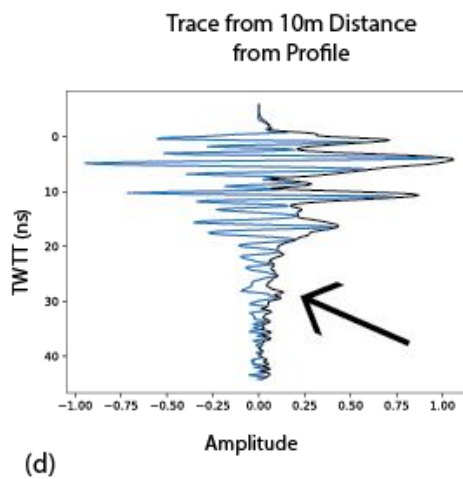
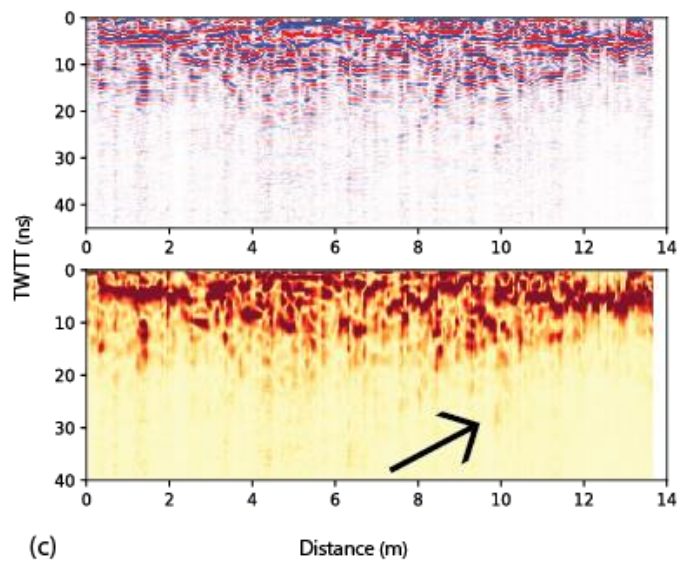


Figure 13: In this figure (a) is identical to Figure 7 except that the diffraction hyperbola picks are not plotted. There is also an arrow that points to a high energy bullseye. However, (b) shows the trace from 10 m in the profile of (a). The blue line is the trace after processing which includes the F-K migration. The black line is the Hilbert transformed trace. Then the black arrow points to an energy package that is also highlighted in (a). In (c) it is the same setup as (a), but it is for line 84 of section 3 of the angular grid. The same energy package is highlighted by an arrow. Then (d) is the same as (b) except it is the 10 m trace from the profile of line 84 from section 3 of the angular grid. Again, the energy package at 30 ns is highlighted by an arrow.

4.3 Depth Maps

Roots were clearly visible on individual profiles but how continuous are these structures? To answer that question, we construct depth sections. Each depth section is constructed by extracting the amplitude of the Hilbert transform and then spatially locating that value within the grid. It is important to note though that the depth sections do not account for topography. To visualize the roots, we also normalize all the values at a given depth by the maximum value found at that depth. Thus, there is a built-in gain at deeper depths. In depth sections, roots that are located at the same depth will be plotted in the same depth sections. Roots that are angled up or down will appear to travel radially outward from the tree in different depth sections.

There are clear and obvious dendritic patterns that emerge from the depth sections (Figure 13). At the shallowest depths individual roots are more difficult to make out, but there is large structures leaving radially from the tree (Figure 13a). At the shallowest depths, up to about 50 cm, finer structures are masked by a constant of higher amplitude, this could be a result of fine roots causing more overall reflectivity or a result of being within the envelop of the direct soil arrival (mostly removed by background filter). After about 60 cm large and complex

branching structures become clear (Figure 13b). At 62 cm below the surface roots can be seen traversing mostly radially away from the tree, but also connecting to one another laterally, especially between x distances of 3-8 m (Figure 13b). These structures appear to be originating from the trunk to root transition (Figure 8a). Although not all depth sections are shown, these narrow and clear features continue down to depths greater than 1 m however they decrease in frequency. At 1.02 m there are only two clear roots remaining (Figure 13c). Both roots appear to originate at the trunk-to-root transition and likely continue out of the survey domain and beyond the canopy (Figure 13c).

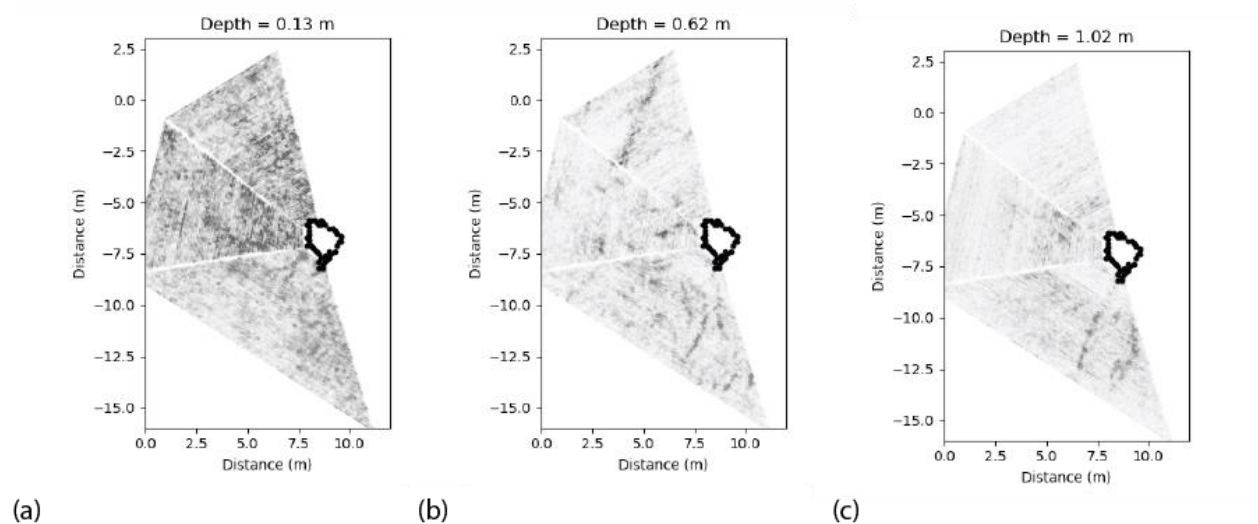


Figure 14: A depth section is shown for three depths in the survey with the x and y axis being the local coordinate system: 0.13 m (a), 0.62 m (b), and 1.02 m (c). In (a) shallow small roots can be viewed in section three close to the trunk. In (b) a clear root can be seen extending directly from the trunk in section 2. Then additionally there is a large network of roots in section 3 at this depth. Then in (c) there are two large roots that extend to the end of the survey length in section 3.

Within the depth sections roots can be located. Being able to combine all the profiles in a radius around the tree is a good way to be able to look at the entire survey on one profile. Figure 14 (a) shows three semicircles around the trunk of the tree where the data from all three sections were combined to create a larger radial profile. A radial profile was created for the 2 m, 4 m, and 6 m radii. Since the profiles are in a semicircle the data is represented in Euclidian degrees. When a root can clearly be tracked from the 2 m radius to the 4 m radius and then additionally to the 6 m radius then the subsurface feature must be a root (Figure 14 (b) to (d)).

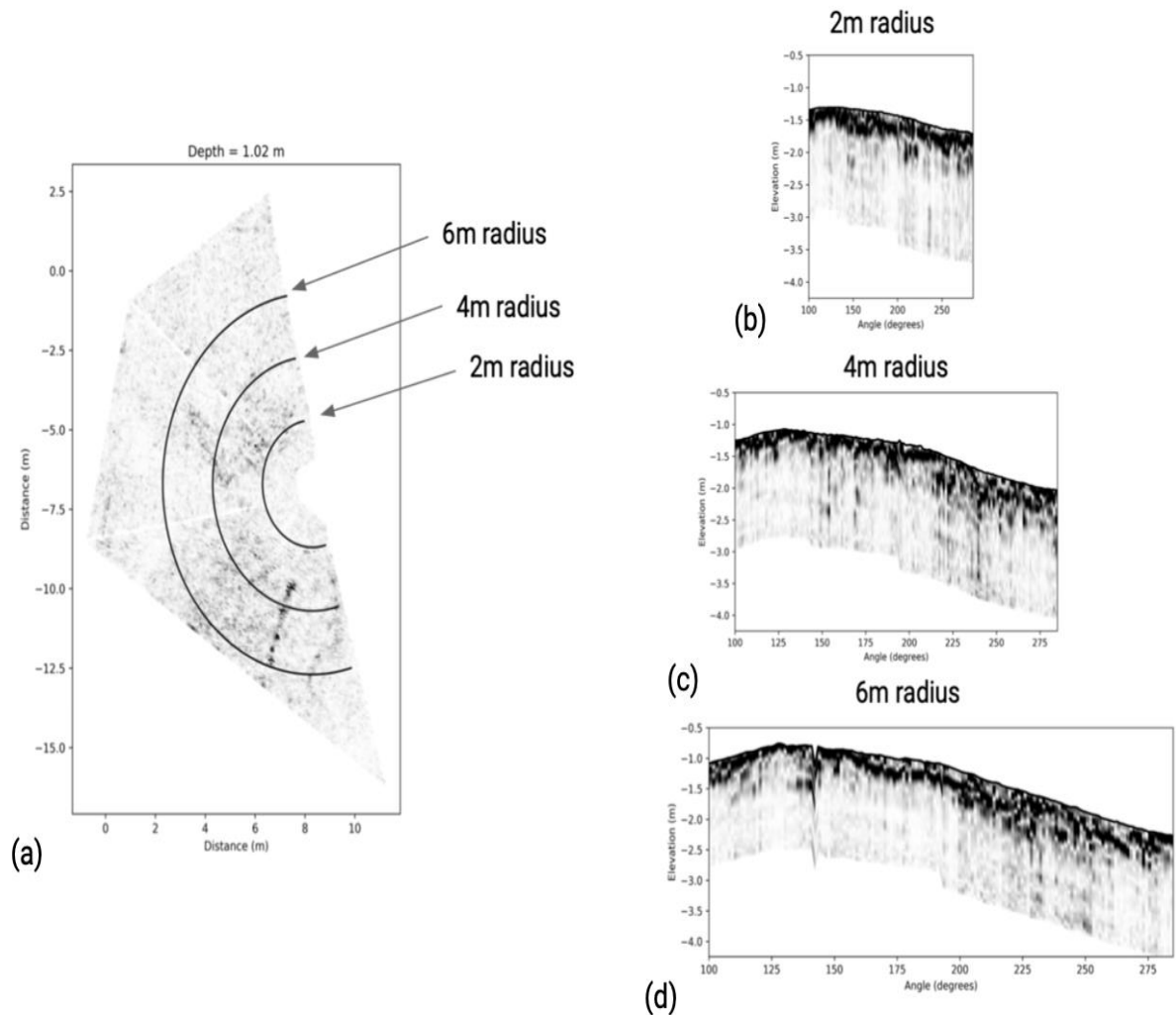


Figure 15: In this figure (a) is the depth section at 1.02 m from Figure 13. The difference being that three circles have been highlighted 2 m, 4 m, and 6 m away from the trunk. On the right these profiles along the circle are shown. The top (b) being the profile from all three sections 2 m away from the tree. Then below that the profile (c) from 4 m away from the trunk is shown. Then the bottom profile (d) is the profiles from 6 m away from the trunk. It is important to note that the x-axis on the profiles is in degrees that correspond to the standard degrees of a circle from the depth section (a). Then the y-axis of the profiles is in depth for the local coordinate system.

While creating the radial profiles does allow for easier comparison of the sections at similar distances from the trunk of the tree, the profiles could continue to improve their ease of comparison with placed in 3D with the topography. When the radial profiles are placed in a correct 3D space, along with the trunk of the tree and the topography, then they can be compared to a depth section at any depth within the survey (Figure 15). When a specific depth section is compared to the radial profiles then the structure of the entire system of roots can be easily seen. In Figure 15 (a) a root feature is seen between 4 to 6 m easting and -9 to -12 m northing. Then in Figure 15 (b) this same root can be seen in the profiles as high energy bullseyes within the 4m radial profile at (8,-8) within the local coordinate system.

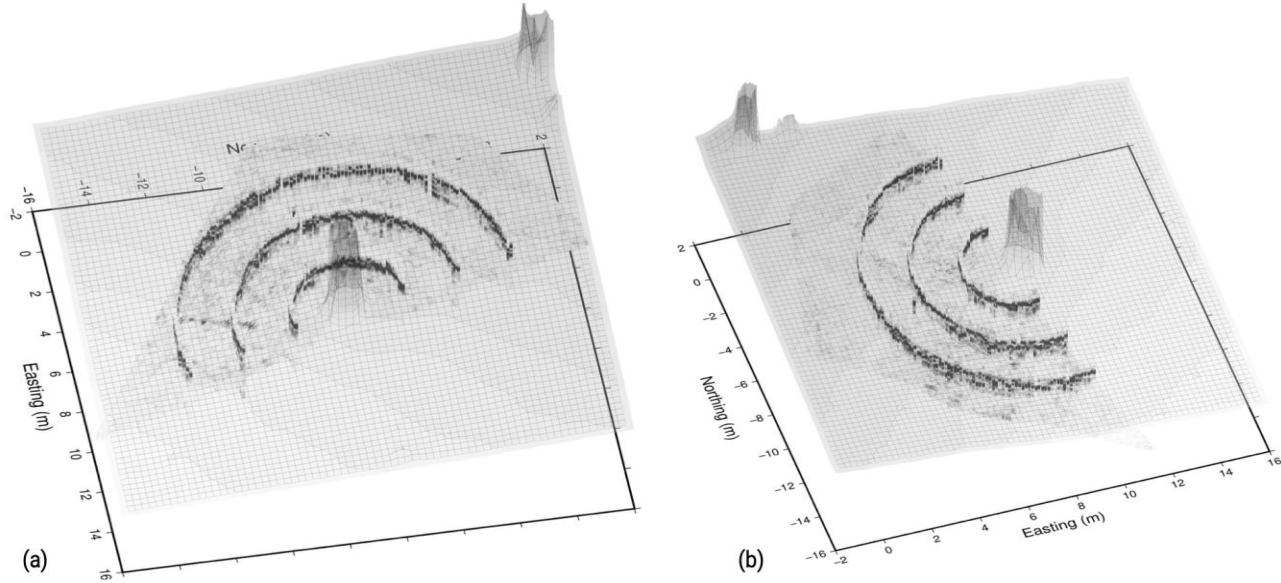


Figure 16: In (a) the depth section at 1.02 m is plotted with topography taken into consideration. Then the semicircles from Figure 14 (a) are shown with the profiles from Figure 14 (b), (c), and (d) are placed within the 3D space in their correct locations. Main roots can be seen in the depth section and then also shown where they intersect with the profiles. In (b) the same image is shown except the angle is different.

Looking through profiles are of interest, there is also value at seeing areas of high density of bullseyes and therefore higher density of roots. This can be done by normalizing to the maximum value within each trace. Doing so, the areas with high density of high energy amplitudes in highlighted. This highlights individual coarse roots (Figure 16) but it also can highlight areas where there could be a high density of finer roots. This is shown in Figure 16 at the interval of 0.00 to -0.25 m in depth for 100 to 150 degrees. This large band of high energy could be a mat of fine roots around the tree.

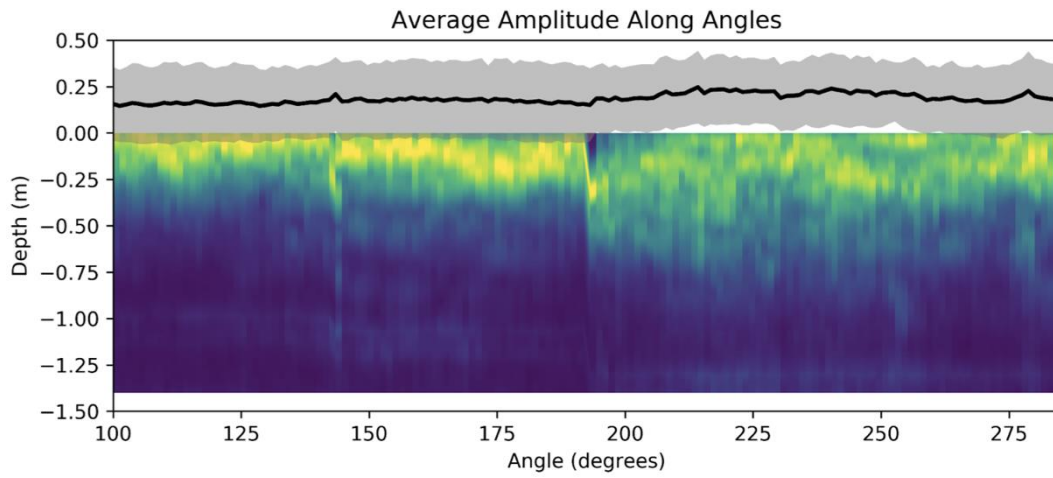


Figure 17: The normalization to the maximum amplitude is shown with the y axis being depth below the subsurface (shown as a negative value). Individual deep coarse roots can be located. For example, one large one at -1.00 m and 255 degrees. Others are visible as well. At the top of the profile there is a large continuous area of high amplitude.

5 Discussion

5.1 Correct Migration Velocities

The correct migration velocities are one of the most important pieces of data within the study. Having the appropriate velocity not only impacts the depth that images are seen at, but it also impacts the imaging as well. To demonstrate this impact, we migrated and transformed our data using three different velocities: 0.065 m/ns, 0.078 m/ns, and 0.091m/ns. The relationship between TWTT and depth (Eq. 6) means that as the velocity increases the reflection, occurring at a given arrival time, would be sourced from a deeper depth. In a sense, higher velocities give the illusion that we see deeper. The same slice in time (13.6 ns) is for the three different velocities have very different depths (Figure 17). We currently lack ground truth data, but the velocity will impact where we expect to encounter tree roots at depth and is thus a very important parameter.

The second, less intuitive, but more important impact the velocity has on the data is improving the resolution (Figure 17). Roots are small structures and already at the lower limit of detection. Since roots clearly show up as diffraction hyperbolas in cross section (Figure 10), it is critical to remove those artifacts through migration. Depth sections of data where the migration velocity is too slow results in very muddled structure (Figure 17a). Roots are still visible, but they are not as defined. As the velocity approaches the ideal velocity (Figure 17b) the root structures become a bit more refined and clearer. Once the correct velocity is selected, root structure emerges and becomes the dominant features in the data (Figure 17c). The depth sections from Figure 17 are all from the same time slice, so the impact on the structure is purely due to the quality of the migration and our ability to remove the diffraction hyperbolas (Figure 17).

The data presented here suggests that the appropriate velocity is the most important parameter with respect to imaging tree roots. Existing studies that have used GPR to study tree roots migrate their data with assumed or tabled values (Hirano et al., 2009) or do not migrate their data at all (Butnor et al., 2001). No migration allows human users to see roots in cross-section, but those cross sections will not translate well to good depth sections. Furthermore, obtaining a good estimate of EM velocity with common offset data is no easy tasks and involves fitting hyperbolas. An alternative suggestion is to take 2-5 common midpoint soundings in each grid. Although our sites did not show variation of velocity with depth, it would not be unreadable to find locations with more than one velocity, in that case it would be critical to find the velocity model and migrate the data accordingly, and not the standard F-K migration.

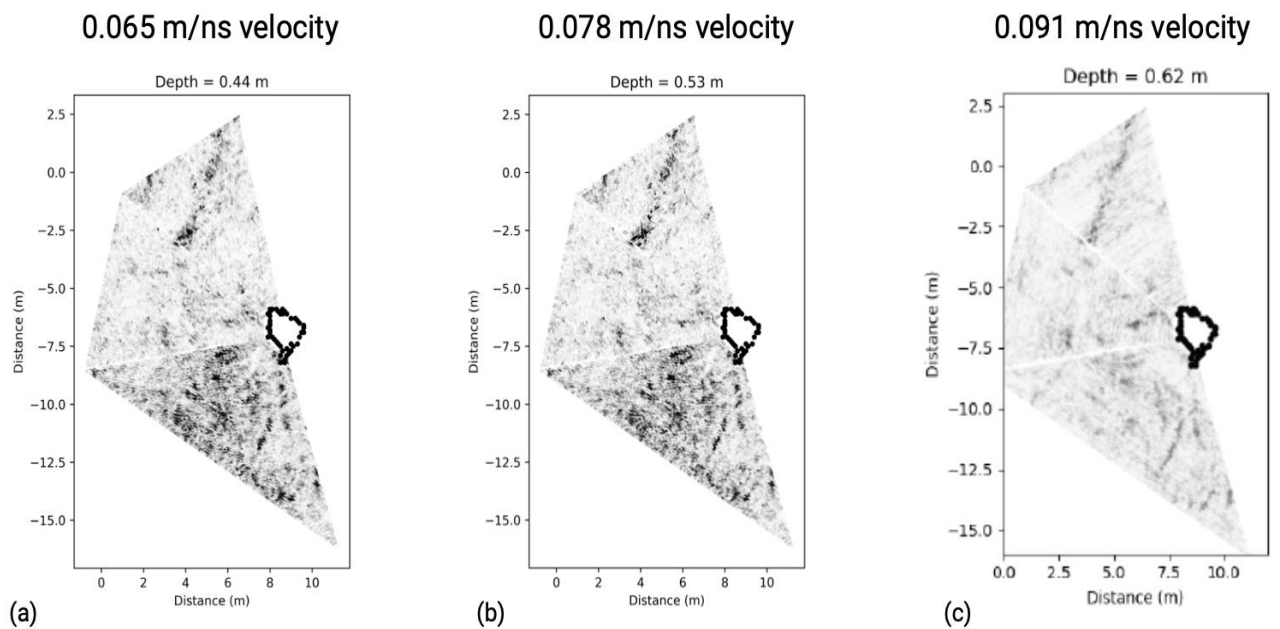


Figure 18: In this figure the same data is presented in (a), (b), and (c) with different migration velocities. This not only affects the imaging but also affects the depth that the data is presented at. The correct depth section from Figure 13 (b) is shown here as (c) with the correct velocity of 0.091 m/ns and depth of 0.62 m. In (a) the depth has been changed from 0.62 m to 0.44 m with the velocity changed to 0.065 m/ns. Then in (b) the depth has been changed to 0.53 m and the velocity was altered to 0.078 m/ns. In both (a) and (b) the prominent roots that are present in (c) can be seen, but finer roots are obscured by the data being migrated with an incorrect velocity.

5.2 What Should We Do to Increase Our Chances of Seeing and Imaging Roots?

In future studies the optimal grid is clearly the angular grid. A circular grid which has been used in studies (Zhu et al., 2014) has the potential to be better in resolution, however it can become tedious to employ. If the angular grid could be used around the entire tree and potentially cut into smaller triangles, then a full tree root map could be constructed. Given the 10 cm spacing the features are most definitely roots and it would be recommended to have tighter line spacing to increase the resolution and the certainty of features in the subsurface.

The benefit of increasing the spacing in between lines is decreasing the time-intensity of a study, but this is at the expense of resolution. With the tighter spacing the resolution is increased but the time-intensity is increased. When in doubt it remains advantageous to have a tighter spacing as it increases the amount of data. Further studies could be done with this survey to optimize the spacing of the lines to better allocate time while still maintaining the resolution of the data.

The antenna used for this study was 500 MHz. The attenuation was 2 m below the subsurface. With the deepest course roots imaged at 1.36 m. This implies that the 500 MHz GPR was adequate as it imaged below the deepest root. However, it would not be recommended to use

a higher MHz GPR unless the maximum rooting depth is not desired to be imaged (Barton & Montagu, 2004)

The tree used in this study is a White Oak tree. This type of tree is known for very laterally extensive roots. Which is ideal for imaging with the GPR. However, many trees have taproots, which due to their vertical features are not ideal for GPR imaging (Butnor et al., 2016). While there may be other geophysical tools that have potential to image vertical features like taproots, GPR does not naturally lend itself to this application.

The environment around the tree is going to impact the imaging of subsurface roots. There are two major factors when talking about the environment: The precipitation or moisture of surrounding soil and then the roots from other nearby trees. In all GPR surveys the moisture content of the soil will affect the imaging of the subsurface due to the difference in the dielectric permittivity between water and soil. It is ideal to do surveys when there is low moisture and there has not been a precipitation event recently. This is especially of importance if the same tree's survey is being split into multiple sections and the data is being collected over a period of days. Then all the sections should aim to have similar moisture contents in the soil and ideally no rain events in the recent days before the survey is conducted. The second main factor in the environment around the survey is the roots from other trees. This may or may not be a factor depending on the goal of the survey. If the study is just looking for subsurface biomass, then it may not matter which tree it comes from, more that it is just within the subsurface. However, if the aim of the survey is to gain insight on the tree roots of a specific tree, then it would be ideal that there are no other trees around the survey area, as the GPR will not be able to distinguish between the origin of roots unless they can be tracked to which trunk they begin at.

5.2 Tree health

In terms of monitoring tree health, we can with confidence map the largest diameter coarse roots. Since root rot is often spread through contact between the root systems of an infected and non-infected tree, the infected tree has the potential to be located and isolated with GPR. When roots rot they will have a similar velocity as the surrounding soil. If a tree was suspected to have a form of root rot, then the roots could be imaged over time and if the roots are “disappearing” under the GPR imaging then it could be deduced that this is a symptom of root rot. If it was decided that the tree was no longer healthy then it could be removed before the root cross with other root systems and therefore minimizing the spread of the disease.

Since GPR is based on the contrasting velocities of the subsurface medium, areas that have higher moisture than the surrounding soil should be able to be tracked as well. This was beyond the scope of this study; however, a survey could be repeated each month per say to see if moisture could be tracked. If this was possible then the moisture uptake from the tree could be seen around the large diameter roots. This comes back to root health because if a root is diseased, it will not be able to uptake the water needed for the tree. Therefore, if a root had a continuous low moisture uptake after functioning normally then it could be suspected of being infected.

5.3 Maximum Depth and Length of Root Maps

Root extended beyond 8.6 m away from the tree, which is beyond the survey length. This 8.6 m boundary was roughly at the dripline of the tree. This means that the coarse roots extend beyond the dripline of the tree. This is shown in Figure 18 (b) and (c) where roots are shown at two separate depths that extend beyond the maximum length of the survey. The deepest imaged

roots were at 1.36 m below the surface as shown in Figure 18 (a). This is within the range that is expected for the maximum rooting depth of a mature White Oak tree.

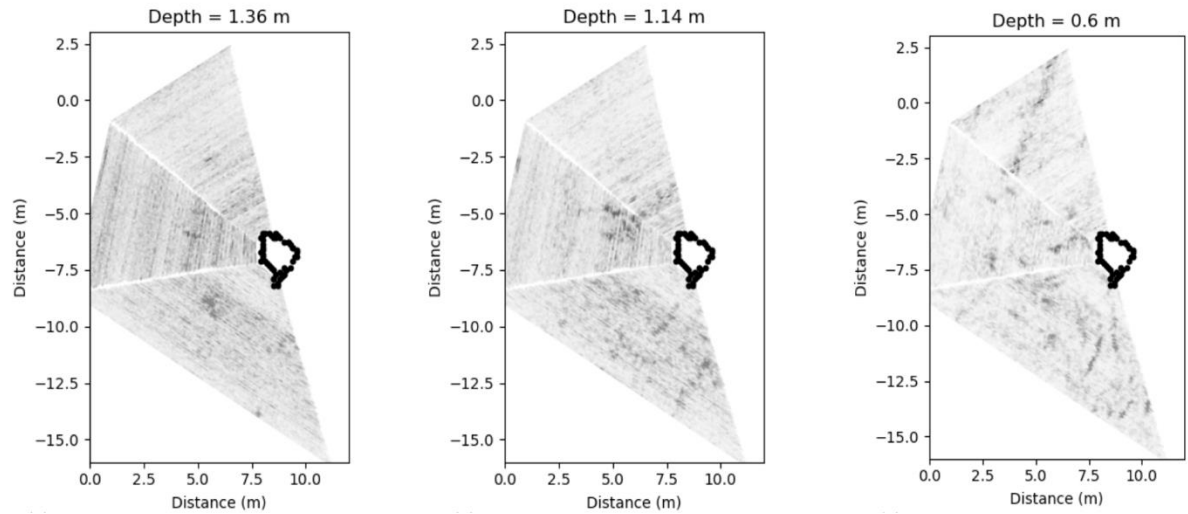


Figure 19: In (a) the depth section for 1.36 m below the subsurface is shown. Linear features that are identified as roots are shown in this depth section but not in the depth sections below it in depth. In (b) and (c) two different depth sections are shown (1.14 m and 0.60 m respectively). Both depth sections have examples of roots that extend beyond the maximum length of the survey which is 8.6 m away from the tree.

5.4 Estimating Biomass

Estimating biomass is an increasingly important topic in the context of carbon storage. Above ground biomass is easily accessible and therefore an estimation for this value can accurately be gained. However, below ground biomass is difficult to estimate due to the roots being buried underground. Equations can be used to estimate subsurface biomass but naturally there is a large error in this method and that error can compound when calculating the below ground biomass for many trees. With GPR surveys the length of the coarse roots can be determined from the depth sections as well as the diameter of the roots from Hilbert Transform

profiles. With the length and diameter of the roots then the volume can be calculated. GPR surveys could be used to better estimate the below ground biomass specific to tree type and environment around the tree.

6 Conclusions

In this study, it was reconfirmed that GPR is a geophysical tool that can be used to map and quantify the tree roots. However, a critical point of getting the highest resolution imaging possible is the velocity analysis. With a correct migration velocity then individual profiles can be processed, and depth sections can be created to show roots within the subsurface.

The velocity analysis is a pivotal point for the entire survey. Having a correct velocity has an influential impact on not only the depths that the roots are seen at but also the quality of the imaging. While an incorrect velocity will not create artificial roots it will obscure features that are within the subsurface. When doing GPR surveys it is imperative to do a velocity analysis, ideally in the early stages of the study.

GPR is also ideal for looking at roots within the subsurface, especially when the data is displayed as depth sections. In this format the maximum rooting length and depth can be seen. In the profiles the diameter of the roots can also be viewed when the Hilbert Transform is applied. With the depth sections and the profiles combined the length of the roots and the diameter can be acquired. Then the volume could be calculated with this information to estimate the biomass of the coarse root system for this tree.

In future work it would be recommended to complete the entire survey so that analysis of the structural network of the tree could be done. This way inferences on how environmental factors (for example: prevailing winds or topography) impact the development of the root system could be made. Additionally, continuing with the biomass estimation would be recommended to be able to utilize the GPR data for better estimations of below ground biomass.

Cited References

- Addo-Danso, S. D., Prescott, C. E., & Smith, A. R. (2016). Methods for estimating root biomass and production in forest and woodland ecosystem carbon studies: A review. *Forest Ecology and Management*, 359, 332–351.
- André, F., Van Leeuwen, C., Saussez, S., Van Durmen, R., Bogaert, P., Moghadas, D., De Resseguier, L., Delvaux, B., Vereecken, H., & Lambot, S. (2012). High-resolution imaging of a vineyard in south of France using ground-penetrating radar, electromagnetic induction and electrical resistivity tomography. *Journal of Applied Geophysics*, 78, 113–122.
- Baker, G. S., Jordan, T. E., & Pardy, J. (2007). *An introduction to ground penetrating radar (GPR)*.
- Barton, C. V., & Montagu, K. D. (2004). Detection of tree roots and determination of root diameters by ground penetrating radar under optimal conditions. *Tree Physiology*, 24(12), 1323–1331.
- Barzaghi, R., Cazzaniga, N. E., Pagliari, D., & Pinto, L. (2016). Vision-based georeferencing of GPR in urban areas. *Sensors*, 16(1), 132.
- Birdsey, R. A., Plantinga, A. J., & Heath, L. S. (1993). Past and prospective carbon storage in United States forests. *Forest Ecology and Management*, 58(1–2), 33–40.
- Bodah, E. T. (2017). Root rot diseases in plants: A review of common causal agents and management strategies. *Agri Res & Tech: Open Access J*, 5(3), 555661.
- Bradford, J. H., Clement, W. P., & Barrash, W. (2009). Estimating porosity with ground-penetrating radar reflection tomography: A controlled 3-D experiment at the Boise Hydrogeophysical Research Site. *Water Resources Research*, 45(4).

- Brantley, S. L., Megonigal, J. P., Scatena, F. N., Balogh-Brunstad, Z., Barnes, R. T., Bruns, M. A., Van Cappellen, P., Dontsova, K., Hartnett, H. E., Hartshorn, A. S., Heimsath, A., Herndon, E., Jin, L., Keller, C. K., Leake, J. R., McDowell, W. H., Meinzer, F. C., Mozdzer, T. J., Petsch, S., ... Yoo, K. (2011). Twelve testable hypotheses on the geobiology of weathering: Hypotheses on geobiology of weathering. *Geobiology*, no-no. <https://doi.org/10.1111/j.1472-4669.2010.00264.x>
- Conyers, L. B. (2013). *Ground-penetrating radar for archaeology*. Altamira Press.
- Ezrari, S., Radouane, N., Tahiri, A., El Housni, Z., Mokrini, F., Özer, G., Lazraq, A., Belabess, Z., Amiri, S., & Lahlali, R. (2022). Dry root rot disease, an emerging threat to citrus industry worldwide under climate change: A review. *Physiological and Molecular Plant Pathology*, 117, 101753.
- Finér, L., Ohashi, M., Noguchi, K., & Hirano, Y. (2011). Factors causing variation in fine root biomass in forest ecosystems. *Forest Ecology and Management*, 261(2), 265–277.
- Forte, E., & Pipan, M. (2017). Review of multi-offset GPR applications: Data acquisition, processing and analysis. *Signal Processing*, 132, 210–220.
- Franco, J. A., & Abrisqueta, J. M. (1997). A comparison between minirhizotron and soil coring methods of estimating root distribution in young almond trees under trickle irrigation. *Journal of Horticultural Science*, 72(5), 797–805.
- Gardner, G. H. F., French, W. S., & Matzuk, T. (1974). Elements of migration and velocity analysis. *Geophysics*, 39(6), 811–825.
- Gracia, V. P., Canas, J. A., Pujades, L. G., Clapés, J., Caselles, O., Garcia, F., & Osorio, R. (2000). GPR survey to confirm the location of ancient structures under the Valencian Cathedral (Spain). *Journal of Applied Geophysics*, 43(2–4), 167–174.

- Hanger, B. C. (1979). The movement of calcium in plants. *Communications in Soil Science and Plant Analysis*, 10(1–2), 171–193.
- Hatch, M. A., Heinson, G., Munday, T., Thiel, S., Lawrie, K., Clarke, J. D., & Mill, P. (2013). The importance of including conductivity and dielectric permittivity information when processing low-frequency GPR and high-frequency EMI data sets. *Journal of Applied Geophysics*, 96, 77–86.
- Hruska, J., Čermák, J., & Šustek, S. (1999). Mapping tree root systems with ground-penetrating radar. *Tree Physiology*, 19(2), 125–130.
- Irianto, R. S. B., Barry, K., Hidayati, N., Ito, S., Fiani, A., Rimbawanto, A., & Mohammed, C. (2006). Incidence and spatial analysis of root rot of *Acacia mangium* in Indonesia. *Journal of Tropical Forest Science*, 157–165.
- Jol, H. M. (1995). Ground penetrating radar antennae frequencies and transmitter powers compared for penetration depth, resolution and reflection continuity¹. *Geophysical Prospecting*, 43(5), 693–709.
- Kaya, A., & Fang, H.-Y. (1997). Identification of contaminated soils by dielectric constant and electrical conductivity. *Journal of Environmental Engineering*, 123(2), 169–177.
- Landsberg, J., & Waring, R. (2017). Water relations in tree physiology: Where to from here? *Tree Physiology*, 37(1), 18–32.
- Lantini, L., Tosti, F., Giannakis, I., Zou, L., Benedetto, A., & Alani, A. M. (2020). An enhanced data processing framework for mapping tree root systems using ground penetrating radar. *Remote Sensing*, 12(20), 3417.
- Li, J., Walubita, L. F., Simate, G. S., Alvarez, A. E., & Liu, W. (2015). Use of ground-penetrating radar for construction monitoring and evaluation of perpetual pavements.

- Natural Hazards*, 75(1), 141–161.
- Li, W., Wen, J., Xiao, Z., & Xu, S. (2018). Application of ground-penetrating radar for detecting internal anomalies in tree trunks with irregular contours. *Sensors*, 18(2), 649.
- Lindström, A., & Rune, G. (1999). Root deformation in plantations of container-grown Scots pine trees: Effects on root growth, tree stability and stem straightness. *Plant and Soil*, 217(1), 29–37.
- Liu, X., Serhir, M., Kameni, A., Lambert, M., & Pichon, L. (2017). Ground penetrating radar data imaging via Kirchhoff migration method. *2017 International Applied Computational Electromagnetics Society Symposium-Italy (ACES)*, 1–2.
- Mabhaudhi, T., Chibarabada, T., & Modi, A. (2016). Water-food-nutrition-health nexus: Linking water to improving food, nutrition and health in Sub-Saharan Africa. *International Journal of Environmental Research and Public Health*, 13(1), 107.
- Mangel, A. R., Moysey, S. M., & Bradford, J. (2020). Reflection tomography of time-lapse GPR data for studying dynamic unsaturated flow phenomena. *Hydrology and Earth System Sciences*, 24(1), 159–167.
- Moser, T. J., & Howard, C. B. (2008). Diffraction imaging in depth. *Geophysical Prospecting*, 56(5), 627–641.
- Neal, A. (2004). Ground-penetrating radar and its use in sedimentology: Principles, problems and progress. *Earth-Science Reviews*, 66(3–4), 261–330.
- Niiyama, K., Kajimoto, T., Matsuura, Y., Yamashita, T., Matsuo, N., Yashiro, Y., Ripin, A., Kassim, A. R., & Noor, N. S. (2010). Estimation of root biomass based on excavation of individual root systems in a primary dipterocarp forest in Pasoh Forest Reserve, Peninsular Malaysia. *Journal of Tropical Ecology*, 26(3), 271–284.

- Noon, D. A., Stickley, G. F., & Longstaff, D. (1998). A frequency-independent characterisation of GPR penetration and resolution performance. *Journal of Applied Geophysics*, 40(1–3), 127–137.
- Norris, J. E. (2005). Root reinforcement by hawthorn and oak roots on a highway cut-slope in Southern England. *Plant and Soil*, 278(1), 43–53.
- Park, B. B., & Yanai, R. (2007). Estimating Root Biomass in Rocky Soils using Pits, Cores, and Allometric Equations. *Soil Science Society of America*, 71(1), 206–213.
<https://doi.org/10.2136/sssaj2005.0329>
- Porsani, J. L., de Matos Jangelme, G., & Kipnis, R. (2010). GPR survey at Lapa do Santo archaeological site, Lagoa Santa karstic region, Minas Gerais state, Brazil. *Journal of Archaeological Science*, 37(6), 1141–1148.
- Repola, J. (2008). *Biomass equations for birch in Finland*.
- Salat, C., & Junge, A. (2010). Dielectric permittivity of fine-grained fractions of soil samples from eastern Spain at 200 MHz. *Geophysics*, 75(1), J1–J9.
- Sochacki, S. J., Ritson, P., Brand, B., Harper, R. J., & Dell, B. (2017). Accuracy of tree root biomass sampling methodologies for carbon mitigation projects. *Ecological Engineering*, 98, 264–274.
- Su-See, L. (1999). Forest health in plantation forests in South-East Asia. *Australasian Plant Pathology*, 28, 283–291.
- Tennant, D. (1975). A test of a modified line intersect method of estimating root length. *The Journal of Ecology*, 995–1001.
- Warren, C., Giannopoulos, A., & Giannakis, I. (2015). An advanced GPR modelling framework: The next generation of gprMax. *2015 8th International Workshop on Advanced Ground*

Penetrating Radar (IWAGPR), 1–4.

Wu, S. Y., Zhou, Q. Y., Wang, G., Yang, L., & Ling, C. P. (2011). The relationship between electrical capacitance-based dielectric constant and soil water content. *Environmental Earth Sciences*, 62, 999–1011.

Xiao, C.-W., Yuste, J. C., Janssens, I. A., Roskams, P., Nachtergale, L., Carrara, A., Sanchez, B. Y., & Ceulemans, R. (2003). Above-and belowground biomass and net primary production in a 73-year-old Scots pine forest. *Tree Physiology*, 23(8), 505–516.

Xie, P., Wen, H., Xiao, P., & Zhang, Y. (2018). Evaluation of ground-penetrating radar (GPR) and geology survey for slope stability study in mantled karst region. *Environmental Earth Sciences*, 77, 1–12.

Zajícová, K., & Chuman, T. (2019). Application of ground penetrating radar methods in soil studies: A review. *Geoderma*, 343, 116–129.

Zenone, T., Morelli, G., Teobaldelli, M., Fischanger, F., Matteucci, M., Sordini, M., Armani, A., Ferrè, C., Chiti, T., & Seufert, G. (2008). Preliminary use of ground-penetrating radar and electrical resistivity tomography to study tree roots in pine forests and poplar plantations. *Functional Plant Biology*, 35(10), 1047–1058.